



# Modulating the bridging units of carbon nitride for highly efficient charge separation and visible-light-responsive photocatalytic H<sub>2</sub> evolution

Dong Liu<sup>a</sup>, Shengtao Chen<sup>a</sup>, Yuexing Zhang<sup>b</sup>, Renjie Li<sup>a,\*</sup>, Tianyou Peng<sup>a,\*</sup>

<sup>a</sup> College of Chemistry and Molecular Sciences, Engineering Research Center of Organosilicon Compounds & Materials, Wuhan University, Wuhan 430072, China

<sup>b</sup> College of Chemistry and Chemical Engineering, Dezhou University, Dezhou 253023, China

## ARTICLE INFO

### Keywords:

Carbon nitride  
Charge separation and transfer  
Molecular heterojunction  
Modulating bridging units  
Photocatalytic H<sub>2</sub> evolution

## ABSTRACT

Carbon nitrides have attracted broad attention in the field of photocatalytic H<sub>2</sub> evolution. However, the design and preparation of carbon nitrides with highly efficient charge separation and transfer are still challenging. Here, we synthesized a novel heptazine derivative-based photocatalyst, named as M+U-x to overcome the inherent limitations of carbon nitrides (C<sub>3</sub>N<sub>4</sub> and C<sub>3</sub>N<sub>5</sub>). Experimental and theoretical calculation results reveal that the resultant M+U-x is composed by electron-withdrawing C<sub>3</sub>N<sub>4</sub> and electron-donating C<sub>3</sub>N<sub>5</sub> moieties, which are integrated into the conjugated framework via N-atoms and azo bridging units to form molecular heterojunctions. Among these, M+U-3 can dramatically facilitate the spatial separation of photoinduced charge carriers, delivering significantly high visible-light-responsive H<sub>2</sub> evolution activity of 372 μmol h<sup>-1</sup> with an AQY of 21.6% at 400 nm. This work provides a novel strategy for rationally modulating the bridging units of carbon nitrides to acquire enhanced charge-carrier mobility and efficient photocatalytic H<sub>2</sub> evolution from the molecular level.

## 1. Introduction

Photocatalytic water splitting that can directly convert sunlight into hydrogen (H<sub>2</sub>) has been considered to be a preeminent economical and eco-friendly H<sub>2</sub> production technology [1]. Although great efforts have been made to rationally design and synthesize photocatalysts, the limited spectral response range, sluggish charge separation/transfer and unsatisfactory photochemical water splitting performance seriously hindered the practical applications of most currently developed photocatalysts [2–7]. In this regard, graphitic carbon nitride (C<sub>3</sub>N<sub>4</sub>) is regarded as one of the most promising photocatalysts for H<sub>2</sub> evolution due to its visible light response and tunable chemical structures, which are not only beneficial to charge transfer, but also provide a broad molecular-level platform for designing metal-free polymer photocatalysts with targeted electronic structures [8–10]. Nevertheless, the main framework of C<sub>3</sub>N<sub>4</sub> is heptazine rings connected by bridging N-atoms that does not participate in the highest occupied molecular orbital (HOMO) or the lowest unoccupied molecular orbital (LUMO) [11,12]. This structural feature makes the charge transfer between adjacent heptazine units hindered by the bridging N-atoms, and thus the behavior of each heptazine unit is almost independent during the

photoreaction processes, which is the reason why C<sub>3</sub>N<sub>4</sub> still displays sluggish charge separation and relatively low photochemical conversion efficiency [11–13].

To surmount those obstacles, N-rich carbon nitrides have been developed by introducing N-atoms into the carbon nitride matrix, which not only helps to alter the electronic and optical properties to narrow the band gap, but also promotes the charge separation/transfer to improve the photoactivity [14–18]. Hereinto, C<sub>3</sub>N<sub>5</sub> composed of azo-linked s-heptazine units possesses broader spectral absorption range and smaller electronic bandgap energy than C<sub>3</sub>N<sub>4</sub>, since the azo-bridging units are conjugated with those heptazine skeletons by the lone pair electrons of azo N-atoms [15,16]. Nevertheless, C<sub>3</sub>N<sub>5</sub> as an attractive carbon nitride photocatalyst just delivers moderate photoactivity due to the still low mobility of photogenerated charge carriers [15,16]. Therefore, it is highly desired to conduct structural modulating on carbon nitrides (C<sub>3</sub>N<sub>4</sub> and C<sub>3</sub>N<sub>5</sub>) to overcome the inherent limitations to develop novel heptazine derivative-based photocatalysts with efficient charge separation and highly active H<sub>2</sub> evolution activity.

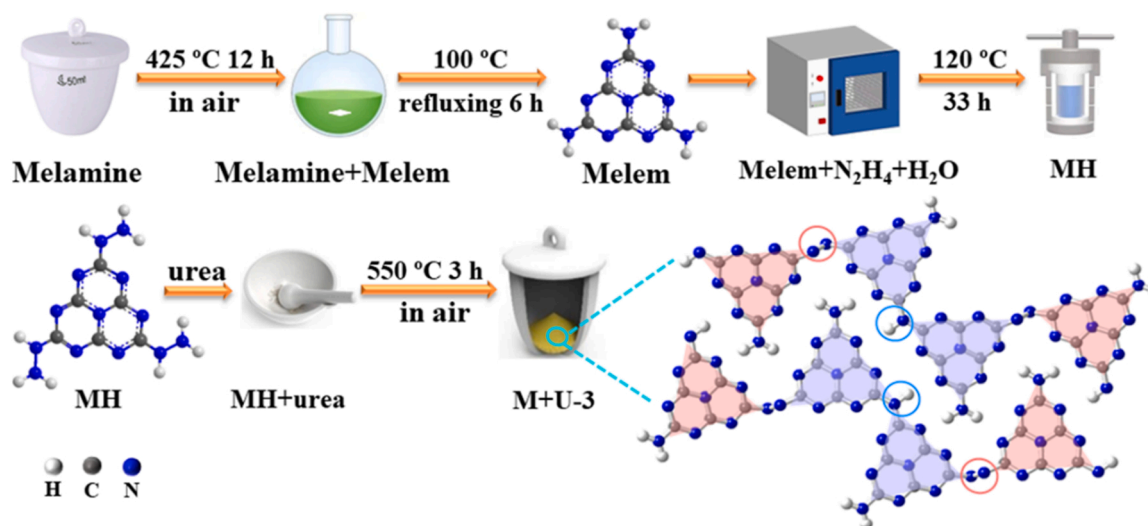
In the great efforts to facilitate the charge separation of polymer photocatalysts, there are several popular strategies such as heterojunction constructing, heteroatom doping and defect engineering

\* Corresponding authors.

E-mail addresses: [lijrj@whu.edu.cn](mailto:lijrj@whu.edu.cn) (R. Li), [typeng@whu.edu.cn](mailto:typeng@whu.edu.cn) (T. Peng).

<sup>1</sup> ORCID: 0000-0001-5780-7022

<sup>2</sup> ORCID: 0000-0002-2527-7634



**Scheme 1.** The synthetic procedures of M+U-*x* molecular heterojunctions.

[19–22]. Thereinto, the construction of molecular heterojunction *via* structural modulating at molecular level is a fairly challenging but charming way to radically inhibit the fast bulk charge recombination of polymer photocatalysts and endow them with unique electrical/optical properties and excellent photocatalytic performance [23–27]. Nevertheless, modulating the bridging mode of heptazine units in carbon nitrides ( $C_3N_4$  and  $C_3N_5$ ) skeletons to construct novel heptazine derivative-based molecular heterojunction for promoting charge separation and boosting  $H_2$  evolution activity has rarely been reported until now.

Recently, we reported that  $C_3N_4$  has stronger interaction with Pt cocatalyst than  $C_3N_5$  in a  $C_3N_4$ /rGO/ $C_3N_5$  system, whereby  $C_3N_4$  and  $C_3N_5$  components realized the reductive and oxidative half-reactions, respectively [15]. The photodeposition experiments imply that  $C_3N_4$  possesses a stronger electron-withdrawing capacity than  $C_3N_5$  even though both of them possess similar composition framework (heptazine), and thus we hypothesized that  $C_3N_4$  and  $C_3N_5$  moieties could be assembled by modulating the bridging mode for facilitating the photo-induced charge separation and transfer. Herein, we report the design, tailored synthesis and characterization of novel carbon nitride molecular heterojunctions composed by  $C_3N_4$  (with N-linked heptazines) and  $C_3N_5$  (with azo-linked heptazines) units (Scheme 1) [15,16], whereby the  $C_3N_4$ / $C_3N_5$  ratio can be readily tuned by controlling the kind and proportion of precursors. To simplify, the prepared molecular heterojunctions are named as M+U-*x*, where M denotes 2,5,8-trihydrazino-*s*-heptazine (MH) [15], U refers to urea, and *x* is the urea mass (g). Among which, M+U-3 with 1.0 wt% Pt cocatalyst delivers the best visible-light-responsive activity and stability with a  $H_2$  evolution rate of  $372 \mu\text{mol h}^{-1}$ , 12.0 and 6.2 times higher than that of the single  $C_3N_4$  ( $31 \mu\text{mol h}^{-1}$ ) and  $C_3N_5$  ( $60 \mu\text{mol h}^{-1}$ ), respectively. Photo(electro)chemical characterizations, *in-situ* CPD measurements and density functional theory (DFT) calculations were conducted to distinctly demonstrate the composition, structure, electronic bandgap energy and the underlying enhancement mechanism of photocatalytic performance. This study not only provides a new avenue for rational design of heptazine derivative-based photocatalysts, but also deepens the understanding of molecular regulation for efficient solar-to-hydrogen conversion.

## 2. Experimental section

### 2.1. Material preparation

Heptazine derivative-based photocatalysts were synthesized *via* a four-step procedure (Scheme 1). Initially, melem (2,5,8-triamino-*s*-

heptazine) was prepared by calcining melamine at 425 °C for 12 h in air followed by refluxing in water for 6 h, which was then treated in an autoclave at 120 °C for 33 h with hydrazine hydrate ( $NH_2-NH_2 \cdot H_2O$ , 55% in water) to transform amino ( $-NH_2$ ) into hydrazino ( $-NH-NH_2$ ) to form melem hydrazine (2,5,8-trihydrazino-*s*-heptazine, named as MH). By grinding 0.10 g MH with different amounts (*x* g) of urea fully, and then the corresponding mixtures were calcined at 550 °C for 3 h with a heating rate of 5 °C  $\text{min}^{-1}$ . The resultant products were named as M+U-*x*, where M denotes MH, U refers to urea and *x* is the urea mass. For example, M+U-3 was prepared from the precursor of 0.10 g MH and 3.0 g urea. All reagents are of analytical grade and used as received without further purification.

Graphitic carbon nitride ( $C_3N_4$ ) was prepared by a urea pyrolysis process in a covered crucible at 550 °C for 2 h with a heating rate of 5 °C  $\text{min}^{-1}$ . To acquire persuasive proof,  $^{15}\text{N}$ -labeled  $C_3N_4$  was prepared using  $^{15}\text{N}$ -labeled urea with the same method, M+U-3( $^{15}\text{N}$ -labeled  $C_3N_4$ ) was prepared by  $^{15}\text{N}$ -labeled urea and MH.  $C_3N_5$  was fabricated *via* a four-step procedure according to our previous report [15]. The physical mixture of  $C_3N_4$  and  $C_3N_5$  was prepared by uniformly grinding  $C_3N_4$  and  $C_3N_5$  with a weight ratio of 3:1, and labeled as  $C_3N_4$ + $C_3N_5$ (3:1). According to the calcination yields of urea (5%) and MH (50%) under the same preparing process as M+U-3 [15], the component of physical mixture  $C_3N_4$ + $C_3N_5$ (3:1) is similar to the M+U-3.

### 2.2. Material characterization

The structural information of the synthesized materials was recorded on a TS10 Fourier transform infrared (FTIR) spectrometer using KBr pellet technique, and the vibrational properties were probed with Raman spectroscopy using a Thermo Scientific iS50 Raman Microscope excited at 1064 nm with tunable incident power of 0.05–0.5 W  $\text{cm}^{-2}$ . Solid-state  $^{13}\text{C}$  nuclear magnetic resonance (NMR) spectra were acquired on a JNM-ECZ600R spectrometer equipped with the cross-polarization magic-angle spinning (CPMAS) technique under a recycle delay of 2.0 s using a spinning frequency of 12 kHz with TMS ( $\delta(^{13}\text{C}) = 0.00 \text{ ppm}$ ) as reference. Solid-state  $^{15}\text{N}$  NMR spectra were obtained on a Bruker AVANCE NEO 400 MHz NMR spectrometer ( $B_0 = 9.39 \text{ T}$ ) equipped with a 4 mm double resonance MAS NMR probe. All solid-state  $^{15}\text{N}$  NMR spectra were acquired under CPMAS conditions using a spinning frequency of 10 kHz with glycine ( $\delta(^{15}\text{N}) = 33.2 \text{ ppm}$ ) reference. Elemental analyses were performed on a Vario EL cube elemental analyzer with CHNS mode.

The crystal phase analyses were conducted based on the X-ray diffraction (XRD) patterns acquired on a Miniflex 600 X-ray

diffractometer with CuK $\alpha$  irradiation ( $\lambda = 0.154178$  nm) working at 40 kV, 15 mA and  $5^\circ \text{ min}^{-1}$  scanning rate. The morphologies were observed on a Zeiss Merlin Compact field emission scanning electron microscope (FESEM). The high-resolution transmission electron microscope (HRTEM) images were obtained on a JEOL LaB $_6$  JEM-2100(HR) high-resolution transmission electron microscope (HRTEM) working at 200 kV. Liquid N $_2$  adsorption-desorption isotherms were measured on an ASAP 2460 nitrogen absorption instrument. All samples were degassed at 120 °C for 24 h before the test. Brunauer-Emmett-Teller (BET) specific surface areas of synthesized materials were determined by a multipoint BET method, and the pore size distributions were determined using desorption branches through the Barrett-Joyner-Halenda (BJH) method.

X-ray photoelectron spectra (XPS) were measured on a Thermo Fisher ESCALAB 250Xi X-ray photoelectron spectroscope equipped with a standard monochromatic source (AlK $\alpha$ ) operated at 300 W. The binding energy of C 1 s core level at 284.8 eV of adventitious carbon was used as the carbon correction value and a standard to calibrate the elements' binding energy. UV-Vis diffuse reflectance absorption spectra (DRS) were recorded at ambient temperature on a Shimadzu UV-3600 UV-Vis-NIR spectrophotometer using BaSO $_4$  as the reference sample. Photoluminescence (PL) spectra were measured on a Hitachi Model F-4500 fluorescence spectrophotometer with an excitation wavelength of 360 nm at room temperature. Time-resolved fluorescence decay spectra (TRFS) were obtained on an Edinburgh FES 920 femtosecond fluorescence spectrophotometer with excited wavelength of 375 nm and detected wavelength of 470 nm at room temperature. Transient photocurrent responses were obtained on a CHI Model 618 C electrochemical workstation via a typical three-electrode system in 0.5 M Na $_2$ SO $_4$  electrolyte under visible light ( $\lambda \geq 400$  nm) illumination. Pt plate and saturated Ag/AgCl electrode ( $E^0 = 0.198$  V vs NHE) were used as counter electrode and reference electrode, respectively. The working electrode was prepared by dropping catalyst suspension (5.0 mg mL $^{-1}$ , dispersed in 0.5 wt% Nafion alcohol solution) on the fluorine tin oxide (FTO) glass ( $1 \times 1 \text{ cm}^2$ ) followed by the solvent volatilization under an infrared lamp. The system was continuously purged by N $_2$  flow for 30 min before irradiation.

Electrochemical impedance spectra (EIS) were performed over the frequency range of 0.01–10000 Hz using a three-electrode system identical to the above transient photocurrent measurements. Besides, the same three-electrode system was used to determine the flat-band potential ( $E_{fb}$ ) based on the impedance-potential values for Mott-Schottky plots. In special, all the above material characterization experiments were conducted at room temperature. For elucidating the charge carrier transfer dynamics, Kelvin probe apparatus (Instytut Fotonowy, Poland) was used to measure the *in-situ* contact potential difference (CPD) of the synthesized materials. Dark and light conditions (an excitation light source of 369 nm) were conducted to achieve the equilibrium condition of carrier transport. The work function ( $W_F$ ) of Pt tip was established to be 4.25 eV. Zeta potentials were acquired on a Zetasizer nano ZS90 instrument (Malvern Panalytical, UK).

### 2.3. Photocatalytic performance test

The photocatalytic H $_2$  generation performance was evaluated in a gas-closed top-irradiation reaction vessel (Pyrex glass) as reported in our previous work [15]. Typically, 50 mg of photocatalyst was dispersed in 50 mL of an aqueous solution containing 10 vol% triethanolamine (TEOA) as sacrificial reagent in the photoreactor. The suspension was subjected to ultrasonic bath treatment for 5 min, vacuumed thoroughly, and then exposed to a 300 W Xe-lamp (PLS-SXE 300, Perfectlight) irradiation with a cutoff filter ( $\lambda \geq 400$  nm) under continuous stirring. The evolved H $_2$  amount was measured via a gas chromatograph (GC, SP 6890, TCD detector, 5 Å molecular sieve columns, and Ar as carrier gas).

The apparent quantum yield (AQY) was measured using a band-pass filter ahead of the 300 W Xe-lamp to attain monochromatic light illu-

mination, which average intensity was evaluated by an Oriol SRC-1000-TC-QZ-N monocrystalline silicon cell. The AQY values were calculated according to Eq. (1) [15]:

$$\begin{aligned} \text{AQY}(\%) &= \frac{\text{number of reacted electrons}}{\text{number of incident photons}} \times 100\% \quad (1) \\ &= \frac{2 \times \text{amount of H}_2 \text{ molecules evolved in unit time}}{\text{number of incident photons in unit time}} \times 100\% \\ &= \frac{2 \times \text{amount of H}_2 \text{ molecules evolved in unit time}}{N} \times 100\% \\ &= \frac{2 \times V \times N_A}{Pt\lambda/hc} \times 100\% \end{aligned}$$

where,  $V$  is the H $_2$  production amount ( $\mu\text{mol}$ ) per hour under different band-pass filters,  $N_A$  is the Avogadro constant ( $6.02 \times 10^{23} \text{ mol}^{-1}$ ),  $h$  is the Plank constant ( $6.626 \times 10^{-34} \text{ J s}^{-1}$ ),  $c$  is vacuum light velocity ( $3 \times 10^8 \text{ m s}^{-1}$ ),  $\lambda$  is the monochromatic light wavelength (nm),  $t$  is the light irradiation time (1 h = 3600 s), and  $P$  is the incident monochromatic light intensity (W), where  $P = p \times A$  (see the following).

The incident photons number ( $N$ ) is obtained by the whole irradiation energy ( $E$ ) in a given time ( $t$ ) divided by the energy of one photon ( $e$ ). Namely,  $N = E/e$ , where  $E = P \times t$ ,  $e = h\nu = hc/\lambda$ , and therefore  $N = Pt\lambda/hc$ . Among which,  $P$  is the irradiation flux (W) on the irradiated area and is equal to the product of the irradiation area ( $A = 25.5 \text{ cm}^2$ ) and the incident monochromatic light intensity ( $p$ , mW/cm $^2$ ) detected by a calibrated monocrystalline silicon cell (SRC-1000-TC-QZ-N, Oriol). The AQY values were calculated at  $\lambda = 350, 400, 420, 450, 520$  and  $570$  nm. Taken the AQY at  $\lambda = 400$  nm as an example, the measured incident monochromatic light intensity is 4.18 mW/cm $^2$ ,  $V = 139 \mu\text{mol h}^{-1}$ ,  $1 \text{ W} = 1 \text{ J s}^{-1}$ , the AQY can be obtained by using the H $_2$  production amount at 400 nm light irradiation.

### 2.4. Theoretical calculations

Density functional theory (DFT) calculations are carried out to investigate the electronic property of C $_3$ N $_4$ , C $_3$ N $_5$  and M+U-3. The single-layer C $_3$ N $_4$  model was built based on the experimental crystal. The single-layer C $_3$ N $_5$  model was built based on the supercell of C $_3$ N $_4$  by modifying atoms and connectivity. The single-layer M+U-3 model was built based on the supercell of C $_3$ N $_4$  and C $_3$ N $_5$  by adjusting certain bridging units. For all models, a vacuum region of 20 Å was used to the  $c$ -axis direction to avoid the influence from neighboring systems. These structures and the cell parameters were then fully optimized adopting Perdew-Burke-Ernzerh (PBE) exchange correlation functional of generalized gradient approximation (GGA) with Grimme's default DFT-D parameters.

The double numeric with polarization functions basis set (DNP) was chosen while the core electrons were treated using Effective Core Potentials (ECP). The convergence criteria for structure optimization were set to: (a) an SCF tolerance of  $1 \times 10^{-5}$  Hartree, (b) an energy tolerance of  $2 \times 10^{-5}$  Hartree, (c) maximum force tolerance of  $2 \times 10^{-3}$  Hartree/Å; and (d) maximum displacement tolerance of  $5 \times 10^{-3}$  Å, (e) thermal smearing of 0.010 Ha, (f) Monkhorst-Pack grid  $k$ -points of  $3 \times 3 \times 1$  [28–30]. The optimized lattices parameters were  $a = 16.5297$  Å,  $b = 7.1077$  Å,  $c = 32.3541$  Å,  $\alpha = \beta = \gamma = 90^\circ$  for C $_3$ N $_4$ ,  $a = 14.2737$  Å,  $b = 29.0157$  Å,  $c = 17.8251$  Å,  $\alpha = \gamma = 90^\circ$ ,  $\beta = 90.692^\circ$  for C $_3$ N $_5$ , and  $a = 13.261$  Å,  $b = 25.1251$  Å,  $c = 16.3072$  Å,  $\alpha = \gamma = 90^\circ$ ,  $\beta = 94.035^\circ$  for M+U-3. The band structures and electronic density of states (DOS) of different materials were calculated based on the optimized structure using the same methods. All DFT calculations were performed using the DMol $^3$  module of BIOVIA Materials Studio 2017 (17.2).

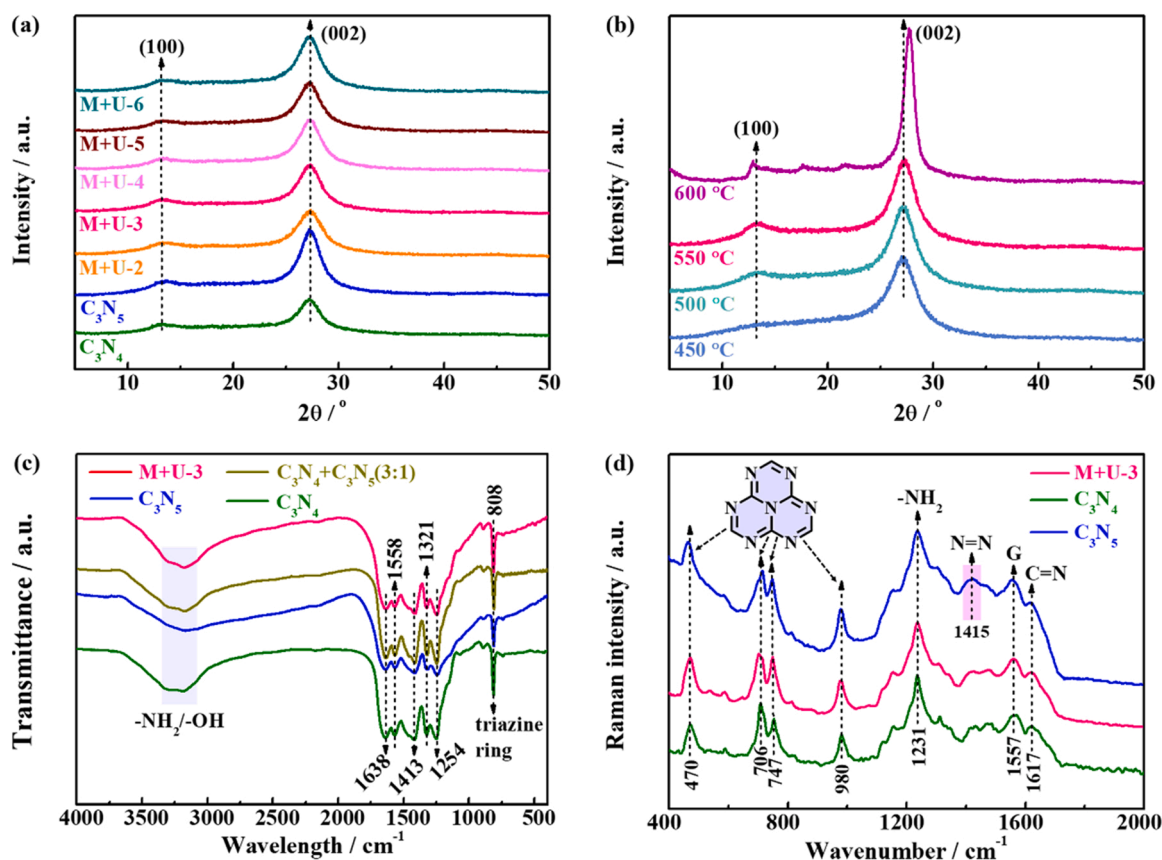


**Fig. 1.** (a,b) XRD patterns of the C<sub>3</sub>N<sub>4</sub>, C<sub>3</sub>N<sub>5</sub> and M+U-*x* (a) and the effect of calcination temperature on the crystallinity of the M+U-3 (b). (c) FTIR spectra of the C<sub>3</sub>N<sub>4</sub>, C<sub>3</sub>N<sub>5</sub>, M+U-3 and the physical mixture (C<sub>3</sub>N<sub>4</sub> + C<sub>3</sub>N<sub>5</sub>) with weight ratio of 3:1. (d) Raman spectra of the C<sub>3</sub>N<sub>4</sub>, C<sub>3</sub>N<sub>5</sub> and M+U-3.

### 3. Results and discussion

#### 3.1. Structure and component analyses

The as-synthesized M+U-*x* molecular heterojunctions show similar X-ray diffraction (XRD) patterns with two characteristic diffraction peaks at  $2\theta = 13.1^\circ$  and  $27.3^\circ$  (Fig. 1a), which are similar to the single C<sub>3</sub>N<sub>4</sub> and C<sub>3</sub>N<sub>5</sub>, and can be ascribed to the in-plane packing of heptazine units of the (100) planes and the interplanar stacking of the (002) planes, respectively [15,21]. By altering the urea addition amounts in 0.10 g MH, those resultant M+U-*x* products display slight differences in the (002) peak intensity. Similarly, the calcination temperature also impacts the crystallinity and even the diffraction peak positions of M+U-3 (Fig. 1b). These results demonstrate that the preparation conditions can affect the crystal phase, component, stacking structure and even the photocatalytic performance of the carbon nitride products, which will be further discussed below.

Fourier transform infrared (FTIR) spectra (Fig. 1c) indicate that all samples display a broad IR band in the range of 3000–3300 cm<sup>-1</sup> assigned to the stretching vibrations of the residual -NH<sub>2</sub>/-NH groups. While those IR bands at 1638, 1413 and 808 cm<sup>-1</sup> can be primarily ascribed to the stretching and bending vibrations of triazine rings. And the C-NH-C units' characteristic vibrations are located at 1254, 1321 and 1558 cm<sup>-1</sup> [15,31,32]. These results verify the successful polymerization to heptazine frameworks of the mixed precursor (MH and urea) at 550 °C. No evident alteration can be observed from those IR spectra of the M+U-3 and the single carbon nitride (C<sub>3</sub>N<sub>4</sub>, C<sub>3</sub>N<sub>5</sub>), which might be due to the retention of the primary structure of heptazine framework. Besides, the physical mixture C<sub>3</sub>N<sub>4</sub> + C<sub>3</sub>N<sub>5</sub>(3:1) has a FTIR spectrum very similar to that of the M+U-3 (Fig. 1c), further confirming that there are similar structures in the C<sub>3</sub>N<sub>4</sub>, C<sub>3</sub>N<sub>5</sub> and M+U-3. Raman

spectra acquired using 1064 nm laser excitation (Fig. 1d) indicate that C<sub>3</sub>N<sub>4</sub> and C<sub>3</sub>N<sub>5</sub> show main Raman peaks at 1617, 1557, 1231, 980, 747, 706 and 470 cm<sup>-1</sup> [16]. Among which, the peaks at 1617, 1557 and 1231 cm<sup>-1</sup> are derived from the vibration mode of C=N, the vibration mode of graphite G-band and the bending mode of attached -NH<sub>2</sub> groups [33,34], respectively. Especially, those Raman peaks at 470, 706, 747 and 980 cm<sup>-1</sup> are attributed to the characteristic fingerprint peaks of heptazine frameworks. Besides, C<sub>3</sub>N<sub>5</sub> displays an obvious Raman band at 1415 cm<sup>-1</sup>, which is absent in the Raman spectrum of C<sub>3</sub>N<sub>4</sub>, can be assigned to the vibration mode of azo (N=N) units [16,35], confirming that C<sub>3</sub>N<sub>5</sub> is composed of azo-linked heptazine units, which is different from C<sub>3</sub>N<sub>4</sub>. As for the M+U-3, a weaker Raman band of N=N unit's vibration mode can also be observed at 1415 cm<sup>-1</sup> even though its intensity is weaker than that of C<sub>3</sub>N<sub>5</sub> as labeled in the pink rectangle (Fig. 1d), indicating that the M+U-3 bearing N=N units has a structure different from the single C<sub>3</sub>N<sub>4</sub> or C<sub>3</sub>N<sub>5</sub>.

Solid-state nuclear magnetic resonance (NMR) spectra were employed to further examine the structural differences among C<sub>3</sub>N<sub>4</sub>, C<sub>3</sub>N<sub>5</sub> and M+U-3. As shown in Fig. 2a, the solid-state <sup>13</sup>C CPMAS NMR spectrum of C<sub>3</sub>N<sub>4</sub> demonstrates two NMR signals at 163.47 and 155.79 ppm, which can be ascribed to the C-atoms of -N=C-(N)<sub>2</sub> and C-(N)<sub>3</sub> units in the heptazine nucleus [16,26], respectively. C<sub>3</sub>N<sub>5</sub> presents <sup>13</sup>C NMR signals of C-atoms in N<sub>2</sub>C-N=N- (at 163.35 ppm) and C-(N)<sub>3</sub> (at 155.79 ppm) units. As for the M+U-3, the <sup>13</sup>C NMR signals locate at 163.32 and 155.73 ppm. These results confirm that C<sub>3</sub>N<sub>4</sub>, C<sub>3</sub>N<sub>5</sub> and M+U-3 have the same heptazine units with almost identical atomic/electronic structures of their C-atom sites. The solid-state <sup>15</sup>N CPMAS NMR spectrum of <sup>15</sup>N-labeled C<sub>3</sub>N<sub>4</sub> displays obvious peaks at 112.14, 136.23 and 190.95 ppm (Fig. 2b), corresponding to the N-atoms of C=N-C, -NH<sub>2</sub> and -NH of the heptazine motif [36–40], respectively. Especially, the <sup>15</sup>N signals of <sup>15</sup>N-labeled C<sub>3</sub>N<sub>4</sub> and C<sub>3</sub>N<sub>5</sub> are nearly



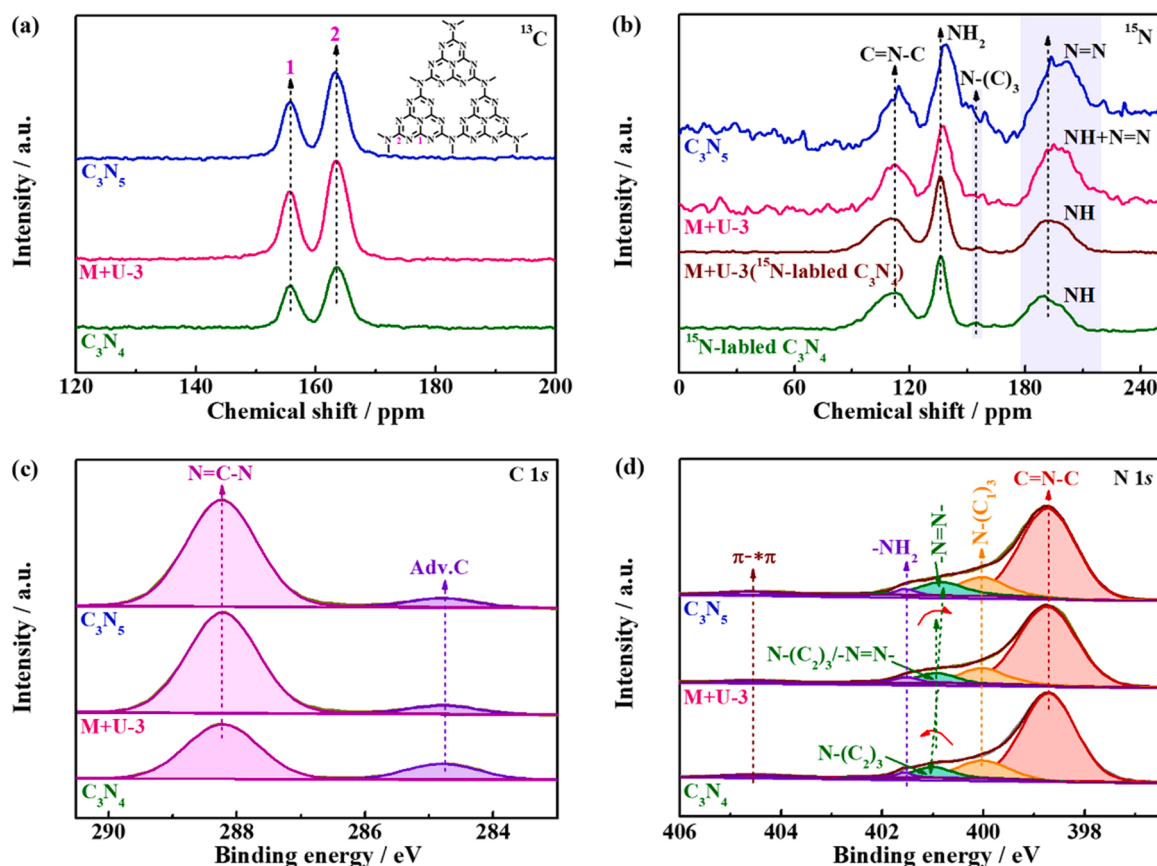


**Fig. 2.** (a) Solid-state  $^{13}\text{C}$  CPMAS NMR spectra of the  $\text{C}_3\text{N}_4$ ,  $\text{C}_3\text{N}_5$  and  $\text{M+U-3}$ . (b) Solid-state  $^{15}\text{N}$  CPMAS NMR spectra of the  $^{15}\text{N}$ -labeled  $\text{C}_3\text{N}_4$  (prepared by  $^{15}\text{N}$ -labeled urea),  $\text{M+U-3}(^{15}\text{N-labeled } \text{C}_3\text{N}_4)$  (prepared by  $^{15}\text{N}$ -labeled urea and MH),  $\text{M+U-3}$  (prepared by urea and MH) and  $\text{C}_3\text{N}_5$  (prepared by MH). (c,d) High-resolution  $\text{C } 1\text{ s}$  (c),  $\text{N } 1\text{ s}$  (d) XPS spectra of the  $\text{C}_3\text{N}_4$ ,  $\text{C}_3\text{N}_5$  and  $\text{M+U-3}$ .

identical (Fig. S1a). The  $^{15}\text{N}$  signals of  $\text{M+U-3}(^{15}\text{N-labeled } \text{C}_3\text{N}_4)$  (112.04, 136.23 and 190.95 ppm) were measured to compare with those of  $^{15}\text{N}$ -labeled  $\text{C}_3\text{N}_4$  and  $\text{M+U-3}$  to determine the influence of  $\text{C}_3\text{N}_5$ . Due to the strong intensity of  $^{15}\text{N}$  signals delivering from  $^{15}\text{N}$ -labeled  $\text{C}_3\text{N}_4$ , the  $^{15}\text{N}$  signals delivering from  $\text{C}_3\text{N}_5$  were almost entirely covered in  $\text{M+U-3}(^{15}\text{N-labeled } \text{C}_3\text{N}_4)$ , leading to a much similar  $^{15}\text{N}$  signals between  $^{15}\text{N}$ -labeled  $\text{C}_3\text{N}_4$  and  $\text{M+U-3}(^{15}\text{N-labeled } \text{C}_3\text{N}_4)$ . While the  $^{15}\text{N}$  signals of  $\text{M+U-3}$  (112.14, 136.86 and 195.70 ppm) display obvious variation compared with those of  $\text{M+U-3}(^{15}\text{N-labeled } \text{C}_3\text{N}_4)$ , indicating the influence of  $\text{C}_3\text{N}_5$  is distinct. Then  $\text{C}_3\text{N}_5$  also presents the NMR signals of N-atoms in  $\text{C=N-C}$  (at 111.67 ppm) and  $\text{-NH}_2$  (at 137.85 ppm) units of the heptazine skeletons. While a much higher chemical shift was observed at 198.89 ppm, which can be attributed to the N-atoms of  $\text{N=N}$  units [15,16,35]. Additionally, the NMR signals of N-atoms in  $\text{N-(C)}_3$  units are also observed in above materials (Fig. 2b), demonstrating that  $^{15}\text{N}$ -labeled  $\text{C}_3\text{N}_4$ ,  $\text{C}_3\text{N}_5$  and  $\text{M+U-3}$  possess identical N-atoms of  $\text{N-(C)}_3$  units of heptazine skeletons. Noticeably, the obvious distinctions in  $^{15}\text{N}$  signals between  $^{15}\text{N}$ -labeled  $\text{C}_3\text{N}_4$  and  $\text{C}_3\text{N}_5$ , indicate the different bridging mode of heptazine units. What's more, the variation trend of  $^{15}\text{N}$  signals delivering from  $\text{-NH/N=N}$  units among

$^{15}\text{N}$ -labeled  $\text{C}_3\text{N}_4$ ,  $\text{M+U-3}$  and  $\text{C}_3\text{N}_5$ , confirming the coexistence of  $\text{C}_3\text{N}_4$  and  $\text{C}_3\text{N}_5$  units in  $\text{M+U-3}$  molecular heterojunction.

The high-resolution  $\text{C } 1\text{ s}$  X-ray photoelectron spectrum (XPS, Fig. 2c) of  $\text{C}_3\text{N}_4$  can be deconvoluted into two binding energy (BE) peaks at 284.8 and 288.2 eV, originating from adventitious C-atoms and aromatic C-atoms of  $\text{N=C-N}$  units that form the  $\text{C}_3\text{N}_4$  framework [16,20], respectively. In addition, except for the adventitious C-atoms (at 284.8 eV), the  $\text{C}_3\text{N}_5$  and  $\text{M+U-3}$  also display a BE peak at 288.2 eV (for  $\text{C}_3\text{N}_5$ ) and 288.1 eV (for  $\text{M+U-3}$ ) of  $\text{N=C-N}$  typed aromatic C-atoms, which are very close to that in the  $\text{C}_3\text{N}_4$  (at 288.2 eV), demonstrating the same basic heptazine units in  $\text{C}_3\text{N}_4$ ,  $\text{C}_3\text{N}_5$  and  $\text{M+U-3}$ . The high-resolution  $\text{N } 1\text{ s}$  XPS spectrum (Fig. 2d) of  $\text{C}_3\text{N}_4$  can be deconvoluted into five BE peaks at 398.7, 400.0, 401.0, 401.5 and 404.6 eV, which can be ascribed to N-species in  $\text{C=N-C}$ ,  $\text{N-(C)}_3$  (connecting the tri-triazine),  $\text{N-(C)}_2$  (bridging the s-heptazine), residual  $\text{-NH}_2$  and satellite peak [16, 20], respectively. Similarly, the  $\text{N } 1\text{ s}$  spectrum (Fig. 2b) of  $\text{C}_3\text{N}_5$  can be fitted to five peaks at 398.7, 400.0, 400.7, 401.5 and 404.6 eV, which are assigned to N-atoms in  $\text{C=N-C}$ ,  $\text{N-(C)}_3$ ,  $\text{N=N}$ , residual  $\text{-NH}_2$  and satellite peak [16], respectively. As for the  $\text{M+U-3}$ , the BE peaks of N-atoms in  $\text{C=N-C}$  (at 398.7 eV) and  $\text{N-(C)}_3$  (at 400.0 eV) display no noticeable variation compared with  $\text{C}_3\text{N}_4$  and  $\text{C}_3\text{N}_5$ , which might be ascribed to the fact that the  $\text{M+U-3}$  possesses the same heptazine units as  $\text{C}_3\text{N}_4$  and  $\text{C}_3\text{N}_5$ . However, the BE peak of N-atoms in  $\text{N-(C)}_2$  (at 400.9 eV) of  $\text{M+U-3}$  shifts ca. 0.1 eV to lower BE position compared with  $\text{C}_3\text{N}_4$ , and shifts ca. 0.2 eV to higher BE position compared with  $\text{C}_3\text{N}_5$ , which might origin from the  $\text{N=N}$  bridging units in  $\text{M+U-3}$ . Additionally, the BE peaks at 401.5 and 404.6 eV are assigned the N-atoms in residual  $\text{NH}_2$  and satellite peak, respectively. The opposite shift direction in BE location of N-atoms in  $\text{N-(C)}_2$  of  $\text{M+U-3}$  indicates its distinct electron behaviors compared with  $\text{C}_3\text{N}_4$  and  $\text{C}_3\text{N}_5$ ,

**Table 1**

Elemental analysis results of the  $\text{C}_3\text{N}_4$ ,  $\text{C}_3\text{N}_5$  and  $\text{M+U-3}$ .

Sample	N (wt %)	C (wt %)	H (wt %)	Experimental formula	C/N (at %) <sup>[a]</sup>
$\text{C}_3\text{N}_4$	59.59	35.96	1.99	$\text{C}_3\text{N}_{4.26}\text{H}_{1.99}$	0.71(0.75)
$\text{C}_3\text{N}_5$	61.86	33.01	1.91	$\text{C}_3\text{N}_{4.82}\text{H}_{2.08}$	0.62(0.60)
$\text{M+U-3}$	60.08	34.02	2.02	$\text{C}_3\text{N}_{4.55}\text{H}_{2.14}$	0.66(-)

<sup>[a]</sup> Datum in parentheses is theoretical value.

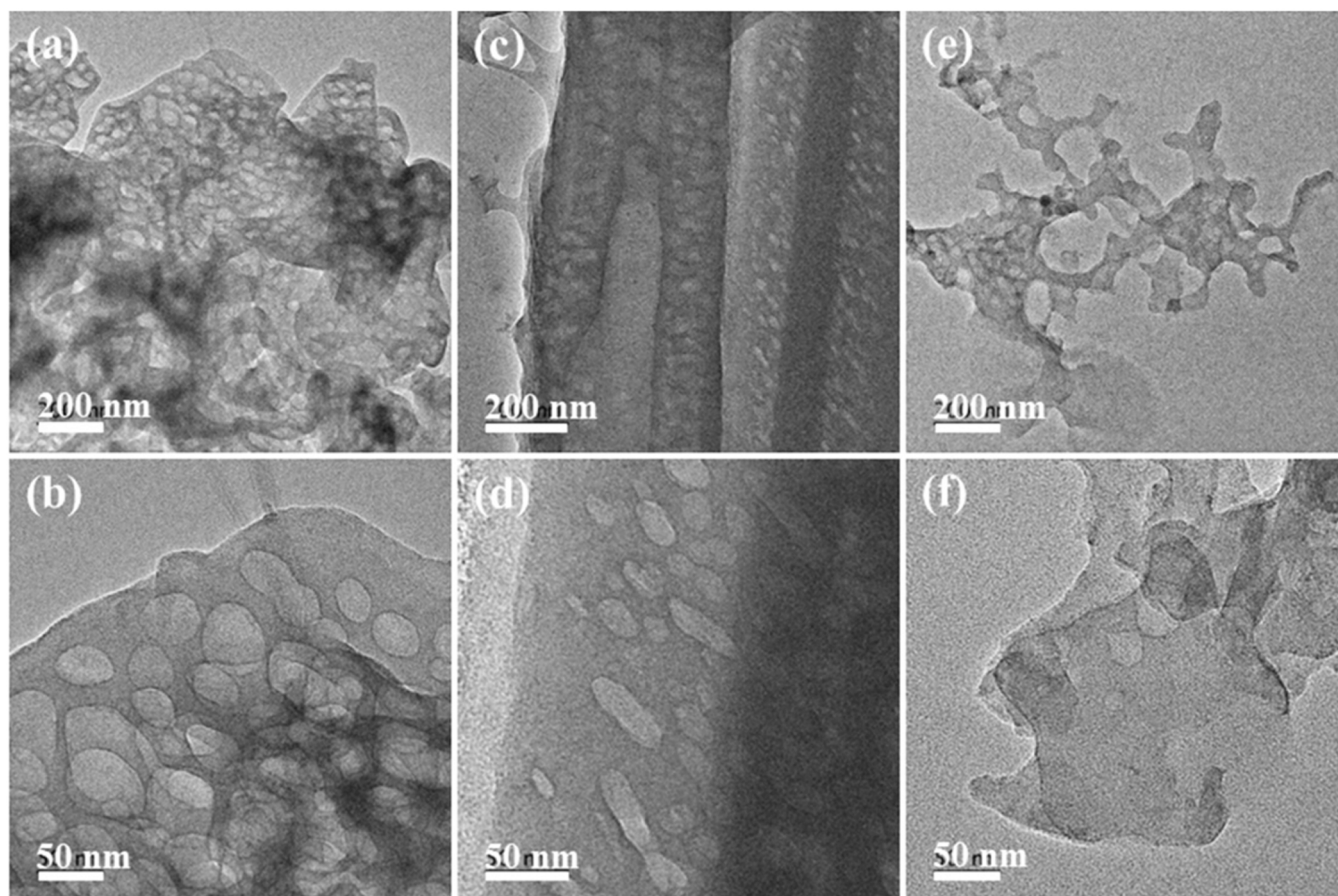


Fig. 3. TEM images of the  $C_3N_4$  (a,b),  $C_3N_5$  (c,d) and M+U-3 (e,f).

further verifying the structure difference among them, which would be conducive to the separation and transfer of photoinduced charge carriers as discussed below. The survey XPS spectra (Fig. S1b) of  $C_3N_4$ ,  $C_3N_5$  and M+U-3 show obvious C 1 s and N 1 s BE peaks in addition to very weak O 1 s peaks that might originate from -OH groups attached at the edge of the polymeric framework [20]. Besides, Pt 4 f BE peaks can also be observed from the Pt/(M+U-3), indicating the successful loading of Pt cocatalyst.

Elemental analysis results (Table 1) display an experimental formula of  $C_3N_{4.26}H_{1.99}$  for  $C_3N_4$ ,  $C_3N_{4.82}H_{2.08}$  for  $C_3N_5$  and  $C_3N_{4.55}H_{2.14}$  for M+U-3. While the C:N atomic ratios are 0.71, 0.62 and 0.66 for  $C_3N_4$ ,  $C_3N_5$  and M+U-3, respectively, slight deviation from theoretical values of  $C_3N_4$  (0.75),  $C_3N_5$  (0.60). Combined with the structures of the synthesized materials, the slight deviations between the predicted and observed C:N ratios might derive from the unbonded  $-NH_2$  at the edge of the carbon nitrides. Notably, the observed hydrogen might arise from  $-NH_2$  and -OH groups attached at the edge of the polymeric framework [16,20].

Based on the above results and discussions on XRD, FTIR, Raman, NMR, XPS and elemental analyses, as well as the fact that M+U-3 was synthesized from urea (the precursor of  $C_3N_4$ ) and MH (the precursor of  $C_3N_5$ ), it can be speculated that the M+U-3 should not be the mixture or composite of  $C_3N_4$  and  $C_3N_5$  but a novel heptazine derivative composed by both  $C_3N_4$  and  $C_3N_5$  moieties to form molecular heterojunction as shown in Scheme 1, which would be conducive to the separation and transfer of photoinduced charge carriers as discussed below.

### 3.2. Microstructure and morphology analyses

TEM images reveal that  $C_3N_4$  displays a curled porous morphology

like spider's web (Fig. 3a,b). The curled morphology is probably derived from the release of large amount of gas during the thermal polymerization of urea. Differently,  $C_3N_5$  presents belt-like morphology (Fig. 3c, d) with dimensions on the micrometer scale. Obvious pores with a diameter ranging from 10 to 50 nm can be observed from those nanobelts. Those pores presented on  $C_3N_4$  and  $C_3N_5$  are beneficial to the subsequent photocatalytic reactions. For M+U-3, curled and crumpled nanosheet-like morphology can be observed (Fig. 3e,f). Compared with M+U-3, the physical mixture  $C_3N_4 + C_3N_5$  (3:1) demonstrates reticular porous morphology like  $C_3N_4$  (Fig. S2). The entirely different morphology of M+U-3 and the physical mixture confirms that M+U-3 is not  $C_3N_4/C_3N_5$  mixture or composite.

Liquid nitrogen adsorption/desorption isotherms and the corresponding pore size distribution plots obtained using the Brunauer-Emmett-Teller (BET) and Barrett-Joyner-Halenda (BJH) methods are summarized in Fig. S3. All samples present type IV-like isotherms with  $H_3$  hysteresis loops at high-pressure region ( $P/P_0 > 0.75$ ), which can be ascribed to the capillary condensation of  $N_2$  molecules among the slit-like pores formed by the particle accumulation [20]. The BJH pore size distribution plots determined from the desorption branches demonstrate that all samples feature broad pore size distributions with peak around 60 nm, ascribed to the particle aggregation. In addition, the small peaks around 3 nm in the pore size distribution plots suggest the coexistence of some mesopores derived from the intra-aggregated pores of small nanoparticles produced by the generated gases during the material preparation process. Especially, the  $C_3N_4$ ,  $C_3N_5$ , M+U-3 and the physical mixture  $C_3N_4 + C_3N_5$  (3:1) shows BET specific surface areas of 36.3, 7.8, 18.1 and 30.1  $m^2 g^{-1}$  (Table S1), respectively. The structural differences between the M+U-3 and the physical mixture result in the alteration in the BET specific surface area.

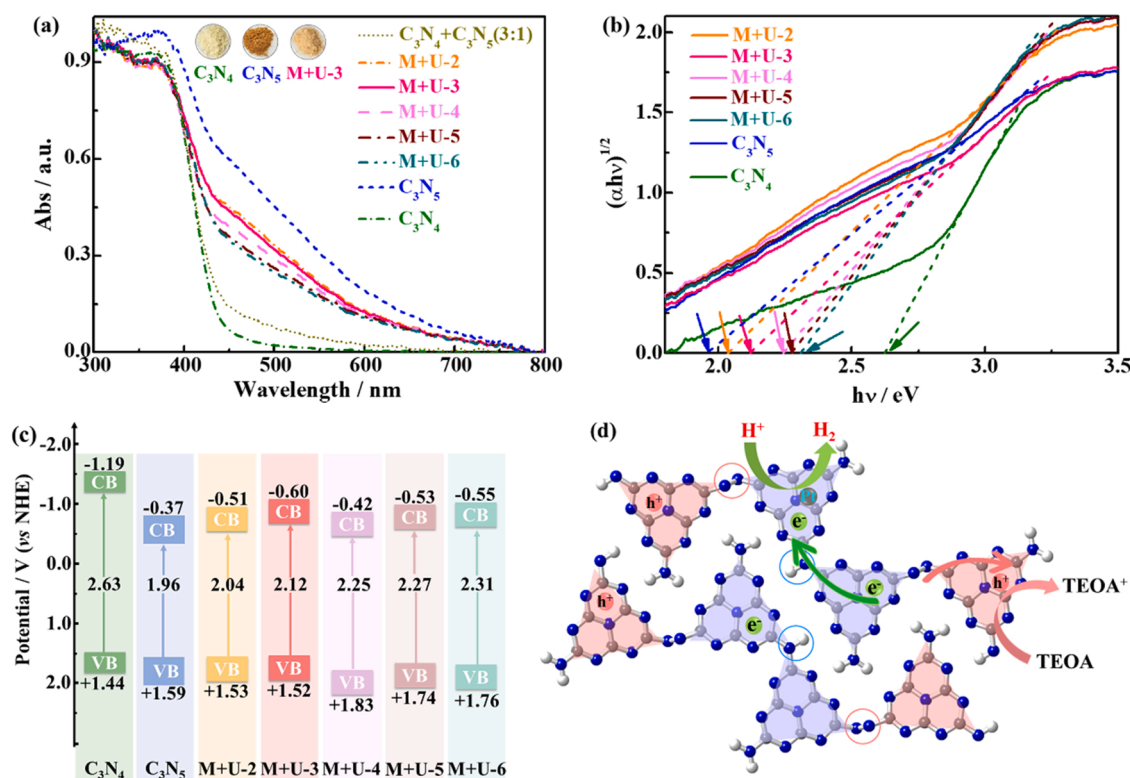


**Fig. 4.** (a) UV-Vis diffuse reflectance absorption spectra (DRS) of the  $C_3N_4$ ,  $C_3N_5$  and M+U- $x$  as well as the physical mixture ( $C_3N_4 + C_3N_5$ ) with a weight ratio of 3:1. (b) Tauc plots of the  $C_3N_4$ ,  $C_3N_5$  and M+U- $x$  calculated from their respective DRS spectra in (a). (c) Schematic illustrating the energy band structures of the  $C_3N_4$ ,  $C_3N_5$  and M+U- $x$ . (d) Illustration of the charge-carrier separation across M+U-3.

### 3.3. Optical property and energy band structure analyses

UV-vis diffuse reflectance spectra (DRS, Fig. 4a) indicate that  $C_3N_4$  shows an intense absorption in the range of 300–400 nm with a tail extending up to ca. 450 nm due to charge transfer from the populated valence band (VB) to the conduction band (CB). The strong absorption can be attributed to the  $\pi \rightarrow \pi^*$  transition of s-triazine/heptazine structures at ca. 330 nm and the  $n \rightarrow \pi^*$  transitions from the nitrogen nonbonding orbital to the aromatic nonbonding orbital at ca. 380 nm [20].  $C_3N_5$  displays a similar abrupt absorption in the range of 300–500 nm with the absorption edge extending up ca. 650 nm, which is assigned to an extended  $\pi$ -conjugated network arising from the overlap between N 2p orbitals in bridging azo moieties and N 2p orbitals in heptazine  $\pi$ -conjugated system [16]. Compared with  $C_3N_4$  and  $C_3N_5$ , the absorption edge of M+U- $x$  (Fig. 4a) mainly inherited the optical features of  $C_3N_4$  and  $C_3N_5$  simultaneously, the absorption edge was slightly blue-shifted with increasing urea content compared with  $C_3N_5$ . However, the stronger absorption in the range of 450–650 nm of M+U-3 is absent in the physical mixture  $C_3N_4 + C_3N_5$ (3:1), also confirming that the M+U-3 is different from the mixture of  $C_3N_4$  and  $C_3N_5$ , and may be composed by bond-linked  $C_3N_4$  and  $C_3N_5$  units to form molecular heterojunctions. From the Tauc plots ( $(\alpha h\nu)^{1/2}$  vs  $h\nu$ ) (Fig. 4b) derived from the DRS curves, where  $\alpha$  is absorption coefficient,  $h$  is plank constant and  $\nu$  is light frequency [20], the optical bandgap energy ( $E_g$ ) of  $C_3N_4$  and  $C_3N_5$  can be calculated to be 2.63 and 1.96 eV, respectively. By altering the urea addition amounts in 0.10 g MH, those resultant M+U-2 (2.04 eV), M+U-3 (2.12 eV), M+U-5 (2.27 eV) and M+U-6 (2.31 eV) display their  $E_g$  values located among those of  $C_3N_4$  and  $C_3N_5$ , also implying that those M+U- $x$  products are composed by  $C_3N_4$  and  $C_3N_5$  moieties.

To accurately determine the band energy structures of the  $C_3N_4$ ,  $C_3N_5$  and M+U- $x$ , Mott-Schottky curves (Fig. S4) were measured. The inverse of their square capacitance ( $C^{-2}$ ) followed a clear linear

correlation with the working potential (vs. Ag/AgCl electrode). Extrapolated intercepts on the potential axis are corresponded to their flat band ( $E_{fb}$ ) levels. Typically, the potential of conduction band ( $E_{CB}$ ) is more negative (ca. 0.1 V) than that of  $E_{fb}$  ( $E_{CB} = E_{fb} + 0.198$ –0.1 V) [15,20]. Thus, the  $E_{CB}$ , the potential of valence band ( $E_{VB}$ ,  $E_{VB} = E_g - E_{CB}$ ) and together with the  $E_g$  values of  $C_3N_4$ ,  $C_3N_5$  and M+U- $x$  are provided (Fig. 4c). The energy band structure of various M+U- $x$  materials indicates that the structure of M+U- $x$  were well-adjusted by controlling the experimental conditions. Especially, the  $E_g$  value of M+U-3 is moderate, on the other hand, the reduction potential of M+U-3 (-0.60 V) is the most negative among all the M+U- $x$  materials. This band structure of M+U-3 renders it highly attractive for photocatalytic hydrogen evolution. Based on the above analysis, the proposed charge-carrier separation and transfer across M+U-3 was displayed in Fig. 4d. Photoexcited M+U-3 delivers photogenerated charge carriers ( $e^-$  and  $h^+$ ) at the conjugated heptazine framework. The electron-withdrawing moieties ( $C_3N_4$ ) and electron-donating moieties ( $C_3N_5$ ) in M+U-3 perfectly direct the transfer of photogenerated charge carriers. Those photogenerated electrons mainly locate at electron-withdrawing  $C_3N_4$  moieties, then captured by Pt to combine with proton to achieve excellent  $H_2$  evolution performance. While those photogenerated holes accumulate at electron-donating  $C_3N_5$  moieties, which are trapped by TEOA to realize oxidative half reaction.

### 3.4. Photocatalytic performance analyses

The photoreaction was conducted by suspending photocatalyst in a triethanolamine (TEOA) aqueous solution (10 vol%) with ultrasonic treatment to obtain a uniform suspension, which was then degassed thoroughly and irradiated with a 300 W Xe-lamp equipped with a 400 nm cutoff filter under continuous stirring. By using M+U-3 as an example photocatalyst, the effect of calcination temperature on the photocatalytic activity was initially investigated. With 1.0 wt% Pt,



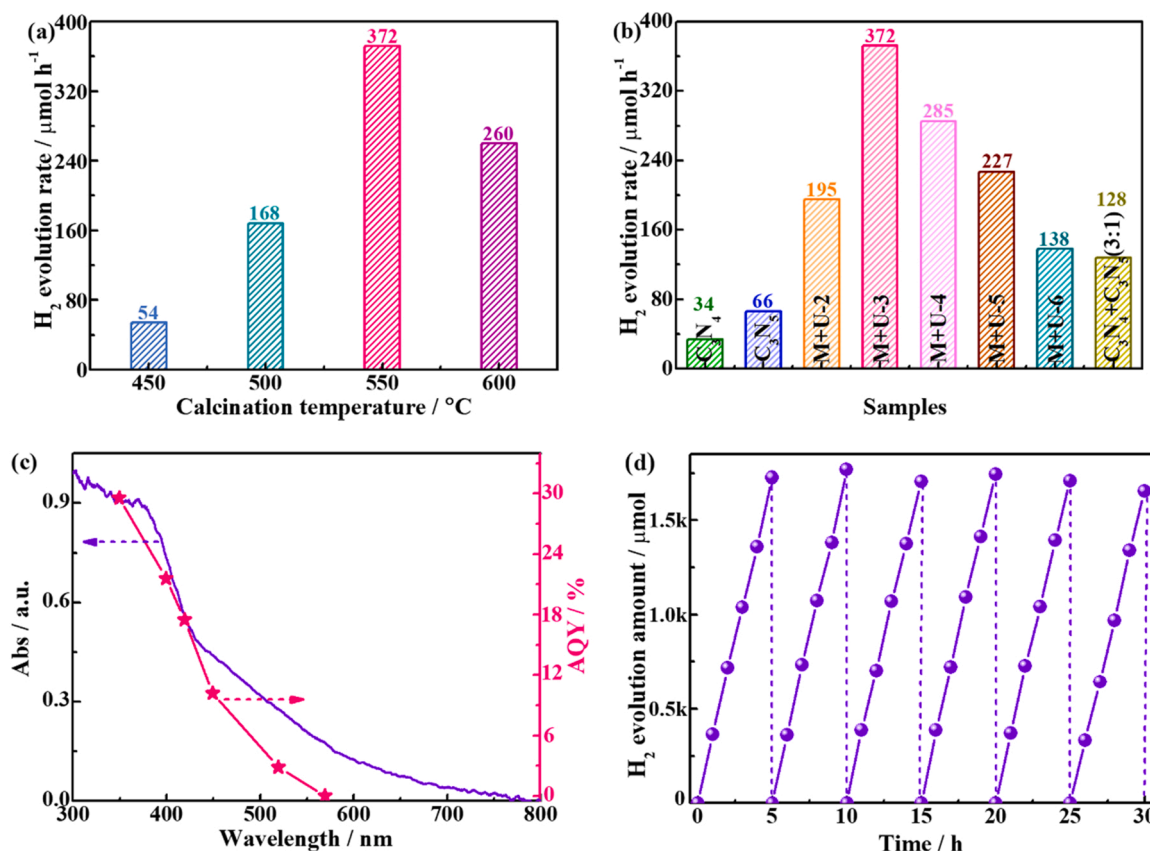


**Fig. 5.** (a) Effects of the calcination temperature on the H<sub>2</sub> generation performance of the M+U-3. (b) H<sub>2</sub> generation performance of the C<sub>3</sub>N<sub>4</sub>, C<sub>3</sub>N<sub>5</sub> and M+U-x as well as the physical mixture (C<sub>3</sub>N<sub>4</sub>+C<sub>3</sub>N<sub>5</sub>) with a weight ratio of 3:1. (c) Wavelength-dependent AQY curve for H<sub>2</sub> generation over the M+U-3. (d) Stability test for H<sub>2</sub> generation of the M+U-3. Conditions: 10 vol% TEOA aqueous solution, 1.0 wt% Pt-loading and  $\lambda \geq 400$  nm light irradiation, if otherwise stated.

M+U-3 derived from calcination at 550 °C delivers the optimal H<sub>2</sub> evolution activity (Fig. 5a), a lower calcination temperature might lead to incomplete polymerization of urea and MH, and a higher one might destroy the structure of M+U-3, and thus resulting in the decreased activity. Additionally, raising or lowering the amount of Pt cocatalyst on M+U-3 derived from calcination at 550 °C also led to inferior photoactivity (Fig. S5a). Similarly, the photocatalytic activity for H<sub>2</sub> evolution was influenced by the dosage of M+U-3 loaded with 1.0 wt% Pt, and 70 mg of photocatalyst presents the highest activity (Fig. S5b). The underlying reasons for the changing trends in the photoactivity along with Pt-loading amount and photocatalyst dosage are likely originated from the decreased penetration depth, severe light scattering and reflection to reduce the light harvesting of photoreaction system.

Under the above optimized material preparation and photoreaction conditions, the photocatalytic H<sub>2</sub> evolution activities of C<sub>3</sub>N<sub>4</sub>, C<sub>3</sub>N<sub>5</sub> and M+U-x were measured and presented in Fig. 5b. As seen, the single-component C<sub>3</sub>N<sub>4</sub> and C<sub>3</sub>N<sub>5</sub> with 1.0 wt% Pt display a photocatalytic H<sub>2</sub> evolution activity of 31 and 60  $\mu\text{mol h}^{-1}$ , respectively. Interestingly, the H<sub>2</sub> evolution performance of M+U-x products follows an order of M+U-3 > M+U-4 > M+U-5 > M+U-2 > M+U-6. That's, the optimal M+U-3 fabricated with 3.0 g urea and 0.10 g MH exhibits the best H<sub>2</sub> evolution rate of 372  $\mu\text{mol h}^{-1}$ , which is about 12.0 and 6.2 times higher than those of C<sub>3</sub>N<sub>4</sub> and C<sub>3</sub>N<sub>5</sub>. Furthermore, the physical mixture C<sub>3</sub>N<sub>4</sub>+C<sub>3</sub>N<sub>5</sub>(3:1) (similar to the synthesized M+U-3) delivers a moderate H<sub>2</sub> evolution activity (128  $\mu\text{mol h}^{-1}$ ) under the same photoreaction conditions (Fig. 5b). This result unambiguously highlighted the structural advantage of the bond-linked molecular heterostructure of M+U-3.

The photocatalytic H<sub>2</sub> evolution activity of M+U-3 loaded with 1.0 wt% Pt was measured under the illumination of monochromatic light with different wavelengths, and the corresponding apparent

quantum yields (AQY) were calculated as a function of the incident light wavelength. As shown in Fig. 5c, the changing trend of AQY value along with the wavelength approximately matches with the DRS spectrum of the M+U-3, suggesting that the H<sub>2</sub> evolution is a light-driven chemical reaction. Specially, the AQY at 400 nm reached 21.6%, suggesting that the present M+U-3 possesses preferable separation/transfer efficiency of photoinduced charge carriers during the photochemical reaction process. The cyclic tests were performed to assess the photocatalytic durability. As shown in Fig. 5d, after 6 continuous cycles (30 h), the photoactivity of M+U-3 only presents a slight decay, which might be due to the TEOA consumption during the long-term photoreaction process. What's more, there is no any significant structure or compositional changes as seen from the comparisons of the XRD patterns, high-resolution C 1 s (b), N 1 s (c) XPS analyses, IR spectra, Raman spectra, solid-state <sup>15</sup>N CPMAS NMR spectra (Fig. S6) and SEM images (Fig. S7) of the Pt/(M+U-3) and its recovered product (recovered Pt/(M+U-3)), further confirming the good stability of M+U-3 during the long-term photoreaction process.

The above results demonstrate that the M+U-3 with 1.0 wt% Pt delivers the optimal visible-light-responsive activity and stability with the H<sub>2</sub> evolution rate of 372  $\mu\text{mol h}^{-1}$ , 12.0 and 6.2 times higher than that of the single C<sub>3</sub>N<sub>4</sub> (31  $\mu\text{mol h}^{-1}$ ) and C<sub>3</sub>N<sub>5</sub> (60  $\mu\text{mol h}^{-1}$ ), respectively. Furthermore, the AQY at 400 nm is up to 21.6%. The photocatalytic performance outperforms most carbon nitride-related photocatalysts reported previously (Table S2), indicating that M+U-3 possesses preferable separation and transfer efficiency of photoinduced charge carriers to boost the photocatalytic H<sub>2</sub> evolution performance, suggesting its promising potential for practical application in the photocatalytic H<sub>2</sub> production.



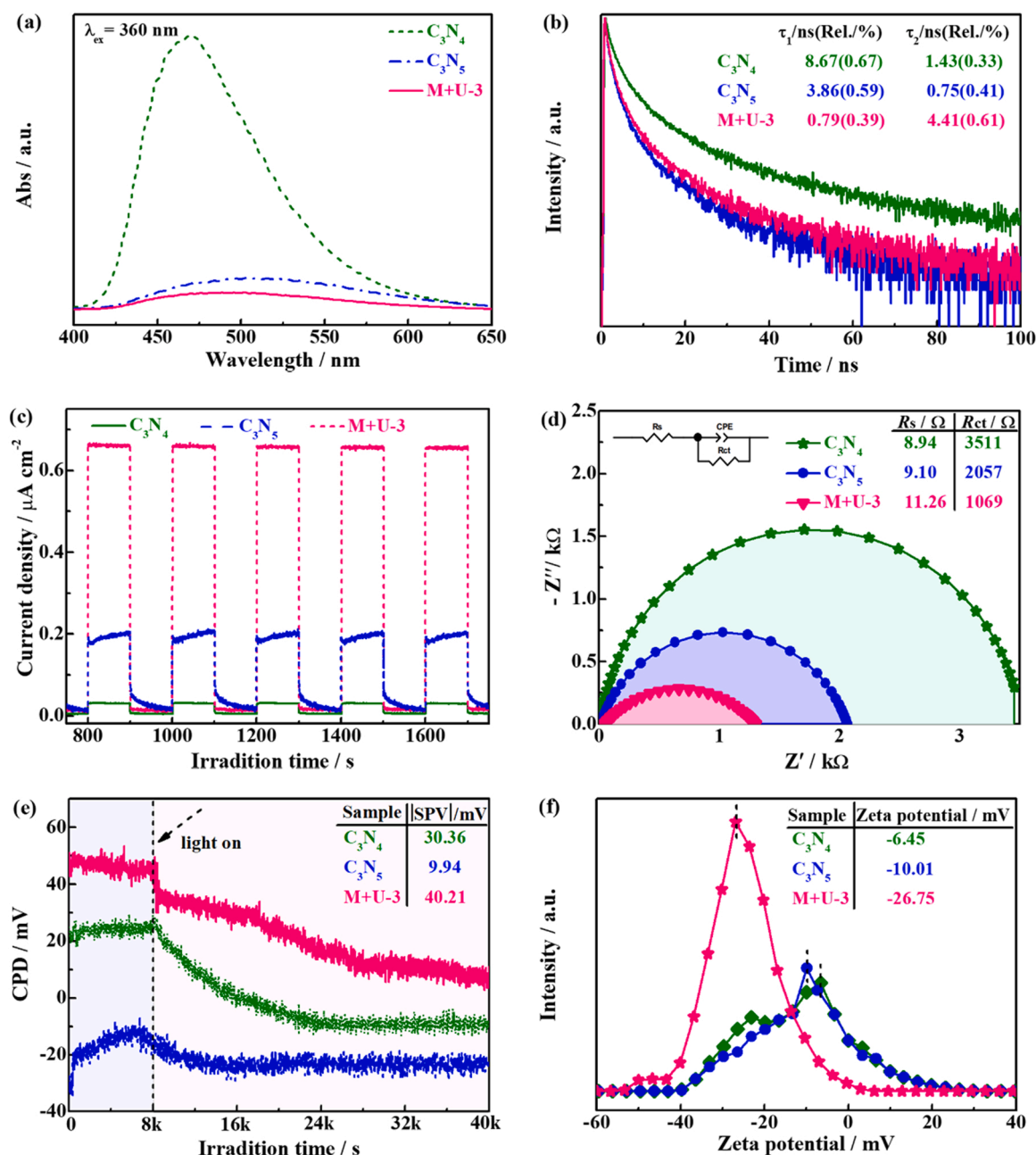


**Fig. 6.** (a,b) Steady-state photoluminescence (PL) spectra (a) and time-resolved fluorescence decay spectra (TRFS, b) of the  $C_3N_4$ ,  $C_3N_5$  and M+U-3. (c,d) Transient photocurrent response curves (c) and electrochemical impedance spectra (EIS, d) of the  $C_3N_4$ ,  $C_3N_5$  and M+U-3. (e) *In situ* CPD curves of the  $C_3N_4$ ,  $C_3N_5$  and M+U-3 in dark and under 369 nm light illumination. (f) Zeta potentials of the  $C_3N_4$ ,  $C_3N_5$  and M+U-3.

### 3.5. Discussion on the photocatalytic mechanism

Photogenerated charge separation and transfer are critical steps during the photochemical conversion processes. Achieving effective charge spatial separation to advance charge utilization efficiency is vital to photocatalytic reactions. Elucidation of photogenerated charge separation and spatial distribution is thus crucial to thoroughly understand the subsequent reaction mechanisms and rationally design efficient photocatalysts. To gain insight into the high performance of M+U-3 and investigate its internal electron transfer dynamics, a series of physicochemical and electrochemical characterizations were conducted.

The photoluminescence (PL) spectra were collected with an excited wavelength of 360 nm to probe the radiative recombination of photo-generated electron-hole pairs. As illustrated in Fig. 6a,  $C_3N_4$  displays a sharp emission peak at 469 nm, which is attributed to fast bulk charge

recombination [41]. While  $C_3N_5$  exhibits remarkably decreased PL intensity compared with  $C_3N_4$  at 500 nm, which can be assigned to efficient charge separation between bulk and surface. As expected, M+U-3 demonstrates the emission peak with the lowest intensity at ca. 500 nm, indicating a superior spatial separation and transfer of photoinduced charge carriers within the molecular heterojunction. The accompanied red-shift of the PL emission peak of  $C_3N_5$  and M+U-3 might derive from the recombination of  $n \rightarrow \pi^*$  transition [42]. The further decreasing peak intensity for M+U-3 manifests its more drastically quenched recombination of photoinduced charge. The time-resolved fluorescence decay spectra (TRFS) were performed employing a picosecond pulsed laser at 375 nm to further probe the charge separation dynamics. The fitted PL lifetime decay curves of  $C_3N_4$ ,  $C_3N_5$  and M+U-3 according to biexponential decay function are displayed in Fig. 6b using the following double-exponential equation [15,20]:

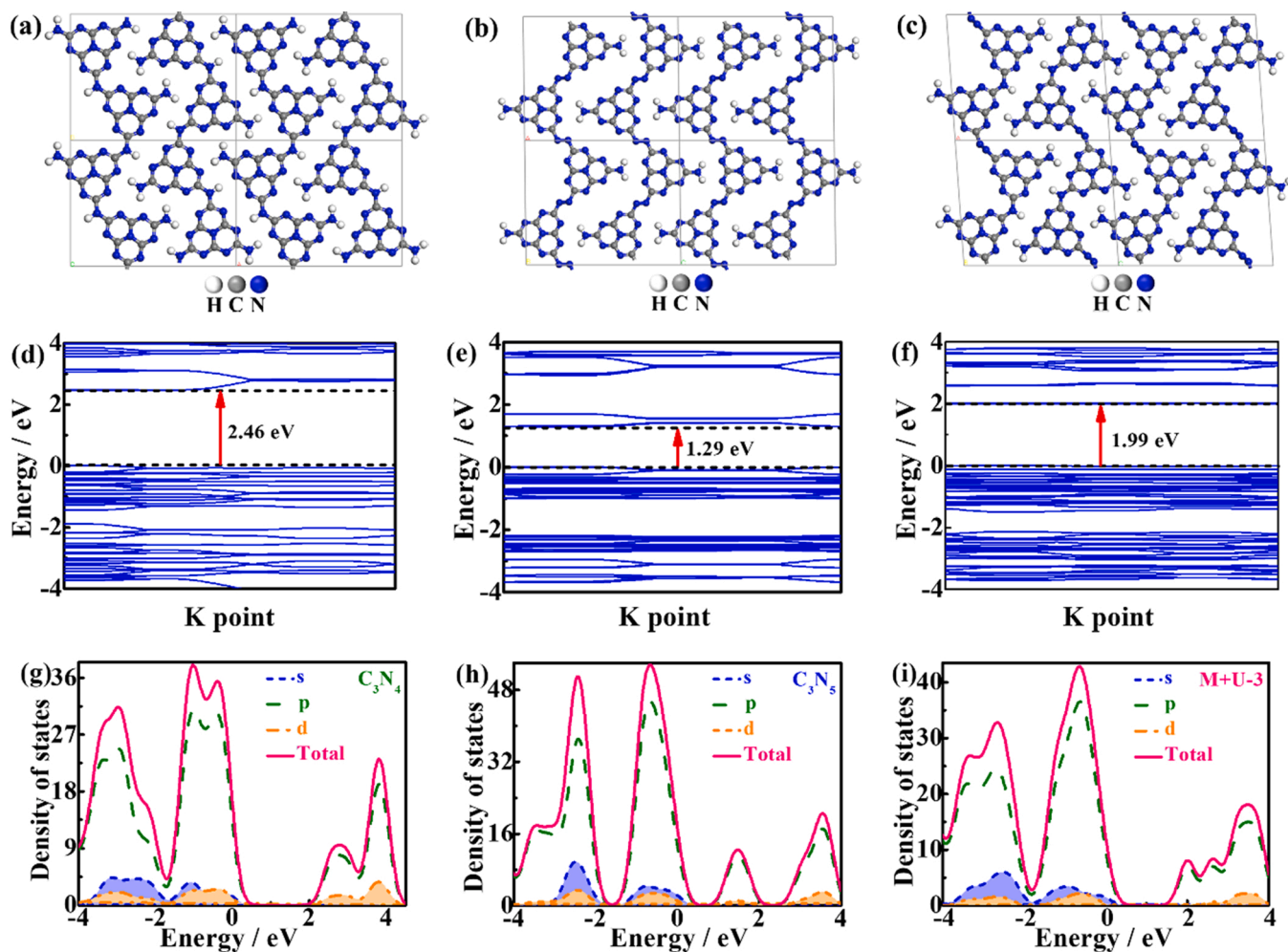


Fig. 7. (a-c) Optimized structure models of the  $C_3N_4$  (a),  $C_3N_5$  (b) and M+U-3 (c). Calculated band structures (d-f) and the corresponding PDOS plots (g-i) of the  $C_3N_4$  (d,g),  $C_3N_5$  (e,h) and M+U-3 (f,i).

$$I_{(t)} = I_0 + A_1 \exp(-t/\tau_1) + A_2 \exp(-t/\tau_2) \quad (2)$$

where,  $I_0$  is the baseline correction value,  $A_1$  and  $A_2$  represent the normalized amplitudes of each decay component,  $\tau_1$  and  $\tau_2$  are the lifetimes (ns) for the radiative and non-radiative recombination processes, respectively.

The specific results of lifetimes and their fractional components are listed in Fig. 6b. The  $C_3N_4$  displays the components of 8.67 ns ( $\tau_1$ ) and 1.43 ns ( $\tau_2$ ) with 67% and 33% contribution, respectively. As for the  $C_3N_5$ , both the radiative ( $\tau_1 = 3.86$  ns with 59% contribution) and non-radiative recombination ( $\tau_2 = 0.75$  ns with 41% contribution) processes are smaller than those of  $C_3N_4$ . Not surprisingly, the fitting values of M+U-3 are 0.79 ns ( $\tau_1$ ) and 4.41 ns ( $\tau_2$ ) with 39% and 61% contribution, respectively. The decreased  $\tau_1$  value suggests significantly suppressed charge recombination. The bigger  $\tau_2$  of M+U-3 might derive from the intersystem crossing (ISC) of electrons from  $\sigma^*$  to  $\pi^*$  orbital followed by nonradiative relaxation, denoting a fast transfer of photo-generated charge carriers [43,44], which was evident from higher percentage contribution of the lifetime component (61%). These dynamic analysis results are consistent with that of the above PL spectra.

Subsequently, chronoamperometry ( $i-t$ ) curves and electrochemical impedance spectra (EIS) were measured to reveal the surface and bulk charge transfer efficiency of the fabricated materials employing the standard three-electrode setup illuminated with visible light ( $\lambda > 400$  nm). As seen from Fig. 6c, M+U-3 possesses much higher

photocurrent density with respect to the single-component  $C_3N_4$  or  $C_3N_5$ , indicating the rapid light response property and fast transfer and separation of photogenerated charge carriers. Under the same condition, M+U-3 shows the most smaller semicircle diameter of the EIS Nyquist plot than  $C_3N_4$  and  $C_3N_5$  (Fig. 6d), reflecting the enhancement of interface charge carrier transfer efficiency in M+U-3.

To further investigate the space separation of charge carriers on M+U-3, the *in-situ* contact potential difference (CPD) of materials at dark and light conditions were measured using Kelvin probe to acquire the surface potential information. Fig. 6e exhibits the stable CPD values of  $C_3N_4$ ,  $C_3N_5$  and M+U-3 under dark and 369 nm light illumination, and the related parameters of surface photovoltage (SPV) can be calculated through the following equations [45]:

$$SPV = CPD_{\text{illumination}} - CPD_{\text{dark}} \quad (3)$$

where  $CPD_{\text{illumination}}$  and  $CPD_{\text{dark}}$  represent the CPD of the materials under dark and light illumination, respectively.

According to the calculated surface characteristic parameters shown in Table S3,  $C_3N_4$  displays a CPD value of 21.33 mV under dark, which change into -9.03 mV under light illumination, leading to a SPV value of 30.36 mV.  $C_3N_5$  demonstrates CPD values of -13.91 and -23.85 mV under dark and light illumination, respectively. It delivers a lower SPV value of 9.94 mV. As for the M+U-3, the CPD value is 47.70 and 7.29 mV under dark and light illumination, generating the highest SPV value of 40.21 mV. These results confirm that rational structural modulating of the heptazine frameworks in molecular level could

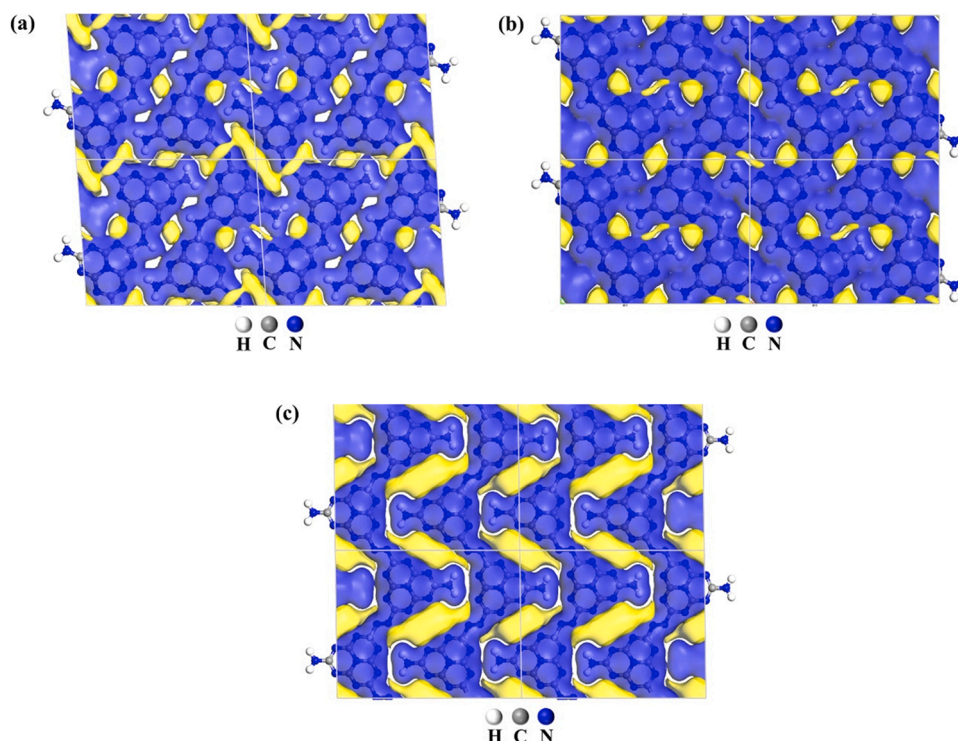


Fig. 8. Electrostatic potential (ESP) distribution maps on the M+U-3 (a),  $C_3N_4$  (b) and  $C_3N_5$  (c).

effectively suppress the recombination of charge carriers.

The adsorption of reactants on the catalyst surface greatly affects the interfacial reaction kinetics, which directly determines the efficiency of photocatalytic reactions. Hence, the affinity toward  $H^+$  on the catalyst surface was investigated using Zeta potential in deionized water. As shown in Fig. 6 f,  $C_3N_4$ ,  $C_3N_5$  and M+U-3 show the Zeta potentials of  $-6.45$ ,  $-10.01$  and  $-26.75$  mV, respectively. The most negative Zeta potential can be recorded over M+U-3 ( $-26.75$  mV), indicating that M+U-3 possesses the strongest electrostatic attraction toward  $H^+$  [46], the structure of M+U-3 is superior to  $C_3N_4$  and  $C_3N_5$ .

All the results and discussions above confirm that the highly efficient separation of charge carriers across the molecular heterostructure was vital to the excellent photocatalytic  $H_2$  production performance of M+U-3. A possible reaction mechanism was proposed as shown in Fig. 4d [26, 27].  $C_3N_4$  units can act as electron-withdrawing moieties to harvest photogenerated electrons,  $C_3N_5$  units can take the charge of electron-donating moieties to accumulate photogenerated holes. Then the mobility of photoinduced charge carriers across the molecular heterostructure was perfectly directed. In this manner, spatial separation of redox sites, superior charge separation and highly efficient  $H_2$  evolution performance were achieved.

### 3.6. Density functional theory (DFT) calculations

To further confirm the molecular structure and investigate the structure-property relationship of the synthesized materials, DFT calculations for the density of states (DOS) are adopted to investigate  $C_3N_4$ ,  $C_3N_5$  and M+U-3 based on the optimized models (Fig. 7a-c). The calculated results demonstrate that the bandgap energy values (Fig. 7d-f) of the  $C_3N_4$ ,  $C_3N_5$  and M+U-3 are 2.46, 1.29 and 1.99 eV, respectively. The bandgap narrowing can be due to the formation of azo-bond in M+U-3 and  $C_3N_5$ , which would derive an extended  $\pi$ -conjugated network arising from the overlap between N 2p orbitals in bridging azo-units and N 2p orbitals in heptazine  $\pi$ -conjugated system [16]. In addition, the bandgap values and the variation trend follow the same trend as the DRS spectra (Fig. 4a,b). Notably, the theoretical  $E_g$  (1.99 eV) of

M+U-3 is very close to the experimental value (2.12 eV), indicating that the theoretical optimized model agrees with the molecular structure predicted *via* experimental data.

The PDOS plots (Fig. 7g-i) of  $C_3N_4$ ,  $C_3N_5$  and M+U-3 indicate that their CB and VB are mainly composed of C 2p and N 2p orbitals. Among which,  $C_3N_5$  (possessing abundant azo-bond, Fig. 7 h) delivers wider orbital overlap population than  $C_3N_4$  (without azo-bond, Fig. 7 g) and M+U-3 (possessing a small number of azo-bond, Fig. 7 i), which may be due to the abundant azo-bond affecting the charge distribution. These DFT calculation results confirm that the amount of azo-bond has a significant effect on the band structure of the synthesized heptazine derivatives. What's more, the speculated molecular structure of M+U-3 was clearly determined.

The electrostatic potential (ESP) distribution maps of the optimized  $C_3N_4$ ,  $C_3N_5$  and M+U-3 models were calculated to further demonstrate the facilitated separation and transportation of the charge carriers, as illustrated in Fig. 8, where blue and yellow colors in ESP maps represent the negative and positive regions, respectively. As seen, in M+U-3 (Fig. 8a), the negative regions mainly locate at  $C_3N_4$  moieties, while the positive ones locate at  $C_3N_5$  moieties, which are beneficial to realize the highly efficient separation of charge carriers to boost the photocatalytic performance. As for  $C_3N_4$  and  $C_3N_5$  (Fig. 8c,d), the charges are uniformly distributed on the whole conjugated framework, which has a great opportunity for charge recombination upon photoexcitation, resulting in severe charge recombination. Additionally, the ESP distribution map in M+U-3 exhibits that the  $C_3N_4$  moiety possesses  $-0.209e$ , which is attractive to  $H^+$ , and  $C_3N_5$  moiety possesses  $+0.209e$ , which is repulsive to  $H^+$ . The results are consistent with the conclusion above that  $C_3N_4$  features electron-withdrawing character,  $C_3N_5$  possesses electron-donating property [47], further verifying the highly separated charge carriers in M+U-3 molecular heterojunction from the point of theoretical calculation.

According to the experimental and DFT calculation results, we can determine that the structure of carbon nitrides can be well tuned *via* the special preparation method above. Especially, M+U-3 possesses a fascinating amount of  $C_3N_4$  and  $C_3N_5$  moieties as electron-withdrawing



and electron-donating units to form molecular heterojunction, which then leads to highly separated charge carriers, further acquiring efficient H<sub>2</sub> evolution performance. The mechanism insight into the excellent photocatalytic H<sub>2</sub> evolution activity of M+U-3 is also proposed as shown in Fig. 4d. Photoexcited M+U-3 leads to photogenerated charge carriers (e<sup>-</sup> and h<sup>+</sup>) across the conjugated heptazine framework. The special structure of M+U-3 perfectly direct the transfer of photogenerated charge carriers. Those photogenerated electrons mainly locates at electron-withdrawing C<sub>3</sub>N<sub>4</sub> moieties, then captured by Pt to combine with proton to achieve excellent H<sub>2</sub> evolution performance. Meanwhile, these photogenerated holes accumulates at electron-donating C<sub>3</sub>N<sub>5</sub> moieties, which are trapped by TEOA to complete the oxidative half reaction. The efficient photocatalytic performance, novel designing and fabricating approach of M+U-3 molecular heterojunction may be instructive for the development of other heptazine derivative-based photocatalysts with more efficient H<sub>2</sub> evolution. Obviously, these findings can also be extended to the other polymeric semiconductors for designing advanced photocatalysts and tuning their photocatalytic conversion efficiency.

#### 4. Conclusion

In summary, a novel heptazine derivative-based photocatalysts (M+U-x molecular heterojunctions) were synthesized by using 2,5,8-trihydrazino-s-heptazine (MH) and urea (U) mixture as the precursor, where C<sub>3</sub>N<sub>4</sub> (with N-linked heptazines) and C<sub>3</sub>N<sub>5</sub> (with azo-linked heptazines) units are integrated into the conjugated frameworks as electron-withdrawing and electron-donating units, respectively. This unique structural feature can overcome the inherent limitations of carbon nitrides (C<sub>3</sub>N<sub>4</sub> and C<sub>3</sub>N<sub>5</sub>), and M+U-3 delivers a significantly higher visible-light-responsive H<sub>2</sub> evolution activity of 372 μmol h<sup>-1</sup> with an apparent quantum yield of 21.6% at 400 nm in contrast to the single C<sub>3</sub>N<sub>4</sub> or C<sub>3</sub>N<sub>5</sub>. Experimental and theoretic calculation results reveal that the resultant M+U-3 composed by C<sub>3</sub>N<sub>4</sub> and C<sub>3</sub>N<sub>5</sub> moieties can facilitate the spatial separation of photoinduced charge carriers, and thus delivering dramatically enhanced photoactivity for H<sub>2</sub> evolution. This study not only provides a new avenue for rational design and synthesis of heptazine derivative-based photocatalysts in molecular level, but also highlights the significance of molecular structure of carbon nitrides to acquire enhanced charge-carrier mobility and efficient solar-powered H<sub>2</sub> evolution.

#### CCRediT authorship contribution statement

**Dong Liu:** Conceptualization, Methodology, Investigation, Writing – original draft preparation. **Shengtao Chen:** Data curation, Investigation. **Yuxing Zhang:** Density functional theory calculations. **Renjie Li:** Data curation, Validation. **Tianyou Peng:** Conceptualization, Writing – review & editing, Supervision. All authors have agreed to the signature to the author list.

#### Declaration of Competing Interest

The authors declare that they have no known competing financial interests or personal relationships that could have appeared to influence the work reported in this paper.

#### Data availability

Data will be made available on request.

#### Acknowledgments

This work was supported by the National Natural Science Foundation of China (22271223, 21975190, 21871215, 21631003 and 21573166), the Science and Technology Planning Project of Shenzhen Municipality

(JCYJ20180302153921190), and the Funds for Innovative Research Groups of Hubei Province (2014CFA007), China. We thank the Core Research Facilities of CCMS (WHU) for the assistance with Solid-State NMR analysis.

#### Appendix A. Supporting information

Supplementary data associated with this article can be found in the online version at doi:10.1016/j.apcatb.2023.122805.

#### References

- [1] Z. Wang, C. Li, K. Domen, Recent developments in heterogeneous photocatalysts for solar-driven overall water splitting, *Chem. Soc. Rev.* 48 (2019) 2109–2125.
- [2] M.Z. Rahman, M.G. Kibria, C.B. Mullins, Metal-free photocatalysts for hydrogen evolution, *Chem. Soc. Rev.* 49 (2020) 1887–1931.
- [3] B. Samanta, A. Morales-García, F. Illas, N. Goga, J.A. Anta, S. Calero, A. Biebele-Hütter, F. Libisch, A.B. Muñoz-García, M. Pavone, M.C. Toroker, Challenges of modeling nanostructured materials for photocatalytic water splitting, *Chem. Soc. Rev.* 51 (2022) 3794.
- [4] X.H. Zhang, T.Y. Peng, S.S. Song, Recent advances in dye-sensitized semiconductor systems for photocatalytic hydrogen production, *J. Mater. Chem. A* 4 (2016) 2365–2402.
- [5] J.M. Wang, L. Xu, T.X. Wang, S.T. Chen, Z. Jiang, R.J. Li, Y.X. Zhang, T.Y. Peng, Porphyrin conjugated polymer with periodic type II-like heterojunctions and single-atom catalytic sites for broadband-responsive hydrogen evolution, *Adv. Funct. Mater.* 31 (2021), 2009819.
- [6] H.H. Young, Y.M. Lee, W. Nam, S. Fukuzumi, Molecular photocatalytic water splitting by mimicking photosystems I and II, *J. Am. Chem. Soc.* 144 (2022) 695–700.
- [7] L.F. Liu, S.W. Du, X.Y. Guo, Y.J. Xiao, Z.X. Yin, N.C. Yang, Y.F. Bao, X.J. Zhu, S. Y. Jin, Z.C. Feng, F.X. Zhang, Water-stable nickel metal-organic framework nanobelts for cocatalyst-free photocatalytic water splitting to produce hydrogen, *J. Am. Chem. Soc.* 144 (2022) 2747–2754.
- [8] X.C. Wang, K. Maeda, A. Thomas, K. Takanabe, G. Xin, J.M. Carlsson, K. Domen, M. Antonietti, A metal-free polymeric photocatalyst for hydrogen production from water under visible light, *Nat. Mater.* 8 (2009) 76–80.
- [9] C.B. Meier, R. Clowes, E. Berardo, K.E. Jelfs, M.A. Zwiñenburgh, R.S. Sprick, A. I. Cooper, Structurally diverse covalent triazine-based framework materials for photocatalytic hydrogen evolution from water, *Chem. Mater.* 31 (2019) 8830–8838.
- [10] Y. Wang, A. Vogel, M. Sachs, R.S. Sprick, L. Wilbraham, S.J. Moniz, R. Godin, M. A. Zwiñenburgh, J.R. Durrant, A.I. Cooper, Current understanding and challenges of solar-driven hydrogen generation using polymeric photocatalysts, *Nat. Energy* 4 (2019) 746–760.
- [11] A. Al-Ahmed, Photocatalytic properties of graphitic carbon nitrides (g-C<sub>3</sub>N<sub>4</sub>) for sustainable green hydrogen production: recent advancement, *Fuel* 316 (2022), 123381.
- [12] B.C. Zhu, L.Y. Zhang, B. Cheng, J.G. Yu, First-principle calculation study of tri-s-triazine-based g-C<sub>3</sub>N<sub>4</sub>: A review, *Appl. Catal. B Environ.* 224 (2018) 983–999.
- [13] V.W. Lau, M.B. Mesch, V. Duppel, V. Blum, J. Senker, B.V. Lotsch, Low-molecular-weight carbon nitrides for solar hydrogen evolution, *J. Am. Chem. Soc.* 137 (2015) 1064–1072.
- [14] Z.H. Xiang, D.P. Cao, L. Huang, J.L. Shui, M. Wang, L.M. Dai, Nitrogen-doped holey graphitic carbon from 2D covalent organic polymers for oxygen reduction, *Adv. Mater.* 26 (2014) 3315.
- [15] D. Liu, J. Yao, S.T. Chen, J. Zhang, R.J. Li, T.Y. Peng, Construction of rGO-coupled C<sub>3</sub>N<sub>4</sub>/C<sub>3</sub>N<sub>5</sub> 2D/2D Z-scheme heterojunction to accelerate charge separation for efficient visible light H<sub>2</sub> evolution, *Appl. Catal. B Environ.* 318 (2022), 121822.
- [16] P. Kumar, E. Vahidzadeh, U.K. Thakur, P. Kar, K.M. Alam, A. Goswami, N. Mahdi, K. Cui, G.M. Bernard, V.K. Michaelis, K. Shankar, C<sub>3</sub>N<sub>5</sub>: A low bandgap semiconductor containing an azo-linked carbon nitride framework for photocatalytic, photovoltaic and adsorbent applications, *J. Am. Chem. Soc.* 141 (2019) 5415–5436.
- [17] G.P. Mane, S.N. Talapaneni, K.S. Lakhi, H. Ilbeygi, U. Ravon, K. Al-Bahily, T. Mori, D.H. Park, A. Vinu, Highly ordered nitrogen-rich mesoporous carbon nitrides and their superior performance for sensing and photocatalytic hydrogen generation, *Angew. Chem. Int. Ed.* 56 (2017) 8481–8485.
- [18] I.Y. Kim, S. Kim, X.Y. Jin, S. Premkumar, G. Chandra, N.S. Lee, G.P. Mane, S. J. Hwang, S. Umapathy, A. Vinu, Ordered mesoporous C<sub>3</sub>N<sub>5</sub> with a combined triazole and triazine framework and its graphene hybrids for the oxygen reduction reaction (ORR), *Angew. Chem. Int. Ed.* 57 (2018) 17135–17140.
- [19] J.W. Fu, J.G. Yu, C.J. Jiang, B. Cheng, G-C<sub>3</sub>N<sub>4</sub>-based heterostructured photocatalysts, *Adv. Energy Mater.* 8 (2017), 1701503.
- [20] D. Liu, S. Zhang, J.M. Wang, T.Y. Peng, R.J. Li, Direct Z-Scheme 2D/2D photocatalyst based on ultrathin g-C<sub>3</sub>N<sub>4</sub> and WO<sub>3</sub> nanosheets for efficient visible-light-driven H<sub>2</sub> generation, *ACS Appl. Mater. Interfaces* 11 (2019) 27913–27923.
- [21] J.S. Zhang, J.H. Sun, K. Maeda, K. Domen, P. Liu, M. Antonietti, X.Z. Fu, X. C. Wang, Sulfur-mediated synthesis of carbon nitride: band-gap engineering and improved functions for photocatalysis, *Energy Environ. Sci.* 4 (2011) 675–678.
- [22] X. Zhang, P.J. Ma, C. Wang, L.Y. Gan, X.J. Chen, P. Zhang, Y. Wang, H. Li, L. H. Wang, X.Y. Zhou, K. Zheng, Unraveling the dual defect sites in graphite carbon



- nitride for ultra-high photocatalytic  $\text{H}_2\text{O}_2$  evolution, *Energy Environ. Sci.* 15 (2022) 830–842.
- [23] H. Cheng, H.F. Lv, J. Cheng, L. Wang, X.J. Wu, H.X. Xu, Rational design of covalent heptazine frameworks with spatially separated redox centers for high-efficiency photocatalytic hydrogen peroxide production, *Adv. Mater.* 34 (2022), 2107480.
- [24] Z.Y. Fang, Y.J. Bai, L.H. Li, D. Li, Y.Y. Huang, R.J. Chen, W.Q. Fan, W.D. Shi, In situ constructing intramolecular ternary homojunction of carbon nitride for efficient photoinduced molecular oxygen activation and hydrogen evolution, *Nano Energy* 75 (2020), 104865.
- [25] S.T. Chen, P.T. Kong, H. Niu, H.R. Liu, X.T. Wang, J. Zhang, R.J. Li, Y.Z. Guo, T. Y. Peng, Co-porphyrin/Ru-pincer complex coupled polymer with Z-scheme molecular junctions and dual single-atom sites for visible light-responsive  $\text{CO}_2$  reduction, *Chem. Eng. J.* 431 (2022), 133357.
- [26] W. Huang, Q. He, Y.P. Hu, Y.G. Li, Molecular heterostructures of covalent triazine frameworks for enhanced photocatalytic hydrogen production, *Angew. Chem. Int. Ed.* 58 (2019) 8676–8680.
- [27] Z.A. Lan, X. Chi, M. Wu, X.R. Zhang, X. Chen, G.G. Zhang, X.C. Wang, Molecular design of covalent triazine frameworks with anisotropic charge migration for photocatalytic hydrogen production, *Small* 18 (2022), 2200129.
- [28] G. Kresse, J. Furthmüller, Efficient iterative schemes for ab initio total-energy calculations using a plane-wave basis set, *Phys. Rev. B* 54 (1996) 11169–11186.
- [29] P.E. Blochl, "Projector augmented-wave method, *Phys. Rev. B* 50 (1994) 17953–17979.
- [30] S. Grimme, Semiempirical GGA-type density functional constructed with a long-range dispersion correction, *J. Comput. Chem.* 27 (2006) 1787–1799.
- [31] P. Niu, L.L. Zhang, G. Liu, H.M. Cheng, Graphene-like carbon nitride nanosheets for improved photocatalytic activities, *Adv. Funct. Mater.* 22 (2012) 4763–4770.
- [32] J. Xu, L. Zhang, R. Shi, Y.J. Zhu, Chemical exfoliation of graphitic carbon nitride for efficient heterogeneous photocatalysis, *J. Mater. Chem. A* 1 (2013) 14766–14772.
- [33] T. Saplinova, V. Bakumov, T. Gmeiner, J. Wagler, M. Schwarz, E. Kroke, 2,5,8-Trihydrazino-s-heptazine: A precursor for heptazine-based iminophosphoranes, *Chem* 635 (2009) 2480–2487.
- [34] S. Tonda, S. Kumar, S. Kandula, V. Shanker, Fe-doped and -mediated graphitic carbon nitride nanosheets for enhanced photocatalytic performance under natural sunlight, *J. Mater. Chem. A* 2 (2014) 6772–6780.
- [35] V. Giulia, V.C. Maria, P. Silvia, S.C. Santiago, Study of the azo-hydrazone tautomerism of acid orange 20 by spectroscopic techniques: UV-Visible, Raman, and surface-enhanced Raman, *Scatt., J. Raman Spectrosc.* 51 (2020) 1295–1304.
- [36] Y.J. Cui, Z.X. Ding, X.Z. Fu, X.C. Wang, Construction of conjugated carbon nitride nanoarchitectures in solution at low temperatures for photoredox catalysis, *Angew. Chem. Int. Ed.* 51 (2012) 11814–11818.
- [37] A. Sattler, S. Pagano, M. Zeuner, A. Zurawski, D. Gunzelmann, J. Senker, K. Müller-Buschbaum, W. Schnick, Melamine-melem adduct phases: investigating the thermal condensation of melamine, *Chem. Eur. J.* 15 (2009) 13161–13170.
- [38] Y.C. Hu, Y. Shim, J. Oh, S. Park, S. Park, Y. Ishii, Synthesis of  $^{13}\text{C}$ ,  $^{15}\text{N}$ -labeled graphitic carbon nitrides and NMR-based evidence of hydrogen-bonding assisted two-dimensional assembly, *Chem. Mater.* 29 (2017) 5080–5089.
- [39] C.Y. Hsu, K.S. Chang, Fabrication and photocatalytic application of aromatic ring functionalized melem oligomers, *J. Phys. Chem. C* 122 (2018) 3506–3512.
- [40] D. Rovnyak, M. Baldus, B.A. Itin, M. Bennati, A. Stevens, R.G. Griffin, Characterization of a carbon-nitrogen network solid with NMR and high field EPR, *Phys. Chem. B* 104 (2000) 9817–9822.
- [41] G.G. Zhang, M.W. Zhang, X.X. Ye, X.Q. Qiu, S. Lin, X.C. Wang, Iodine modified carbon nitride semiconductors as visible light photocatalysts for hydrogen evolution, *Adv. Mater.* 26 (2014) 805–809.
- [42] F.T. He, X.M. Liu, X.L. Zhao, J.Q. Zhang, P. Dong, Y. Zhang, C.C. Zhao, H.Q. Sun, X. G. Duan, S.B. Wang, S.J. Wang, Manipulation of  $n \rightarrow \pi^*$  electronic transitions via implanting thiophene rings into two-dimensional carbon nitride nanosheets for efficient photocatalytic water purification, *J. Mater. Chem. A* 10 (2022) 20559–20570.
- [43] L.C. Chen, C.Y. Teng, C.Y. Lin, H.Y. Chang, S.J.H. Teng, Architecting nitrogen functionalities on graphene oxide photocatalysts for boosting hydrogen production in water decomposition process, *Adv. Energy Mater.* 6 (2016), 1600719.
- [44] R. Shi, Z. Li, H. Yu, L. Shang, C. Zhou, G.I. Waterhouse, L.Z. Wu, T. Zhang, Effect of nitrogen doping level on the performance of N-doped carbon quantum dot/ $\text{TiO}_2$  composites for photocatalytic hydrogen evolution, *ChemSusChem* 10 (2017) 4650–4656.
- [45] J.J. Zhang, L.X. Wang, C.H. Jiang, B. Cheng, T. Chen, J.G. Yu,  $\text{CsPbBr}_3$  nanocrystal induced bilateral interface modification for efficient planar perovskite solar cells, *Adv. Sci.* 8 (2021), 2102648.
- [46] P. Zhang, D.R. Sun, A. Cho, S. Weon, S. Lee, J. Lee, J.W. Han, D.P. Kim, W. Choi, Modified carbon nitride nanosheet as bifunctional glucose oxidase-peroxidase for metal-free bioinspired cascade photocatalysis, *Nat. Commun.* 10 (2019) 940.
- [47] Z.X. Ma, X.P. Zong, Q. Hong, L.J. Niu, T.Y. Yang, W.S. Jiang, D. Qu, L. An, X. Y. Wang, Z.H. Kang, Z.C. Sun, Electrostatic potential of the incorporated asymmetry molecules induced high charge separation efficiency of the modified carbon nitride copolymers, *Appl. Catal. B Environ.* 319 (2022), 121922.